CrossMark

TECHNICAL PAPER

Thermal analysis of anti-icing systems in aeronautical velocity sensors and structures

J. R. B. de Souza[1] · K. M. Lisboa[1] · A. B. Allahyarzadeh[1] · G. J. A. de Andrade[1] ·
J. B. R. Loureiro[1] · C. P. Naveira-Cotta[1] · A. P. Silva Freire[1] · H. R. B. Orlande[1] ·
G. A. L. Silva[2] · R. M. Cotta[1]

Abstract This work reviews theoretical–experimental studies undertaken at COPPE/UFRJ on conjugated heat transfer problems associated with the transient thermal behavior of heated aeronautical Pitot tubes and wing sections with anti-icing systems. One of the main objectives is to demonstrate the importance of accounting for the conduction–convection conjugation in more complex models that attempt to predict the thermal behavior of the anti-icing system under adverse atmospheric conditions. The experimental analysis includes flight tests validation of a Pitot tube thermal behavior with the military aircraft A4 Skyhawk (Brazilian Navy) and wind tunnel runs (INMETRO and NIDF/COPPE/UFRJ, both in Brazil), including the measurement of spatial and temporal variations of surface temperatures along the probe through infrared thermography. The theoretical analysis first involves the proposition of an improved lumped-differential model for heat conduction along a Pitot probe, approximating the radial temperature gradients within the metallic and ceramic (electrical insulator) walls. The convective heat transfer problem in the external fluid is solved using the boundary layer equations for compressible flow, applying the Illingsworth variables transformation considering a locally similar flow. The nonlinear partial differential equations are solved using the Generalized Integral Transform Technique in the *Mathematica* platform. In addition, a fully local differential conjugated problem model was proposed, including both the dynamic and thermal boundary layer equations for laminar, transitional, and turbulent flow, coupled to the heat conduction equation at the sensor or wing section walls. With the aid of a single-domain reformulation of the problem, which is rewritten as one set of equations for the whole spatial domain, through space variable physical properties and coefficients, the GITT is again invoked to provide hybrid numerical–analytical solutions to the velocity and temperature fields within both the fluid and solid regions. Then, a modified Messinger model is adopted to predict ice formation on either wing sections or Pitot tubes, which allows for critical comparisons between the simulation and the actual thermal response of the sensor or structure. Finally, an inverse heat transfer problem is formulated aimed at estimating the heat transfer coefficient at the leading edge of Pitot tubes, in order to detect ice accretion, and estimating the relative air speed in the lack of a reliable dynamic pressure reading. Due to the intrinsic dynamical behavior of the present inverse problem, it is solved within the Bayesian framework by using particle filter.

This work is dedicated to the 228 victims of the AF447 flight and their families. This hard lesson will hopefully affect somehow technology development protocols, in a progressively more competitive world, reminding us all that there is no acceptable, sustainable, and safe technological development without a supporting extensive scientific analysis.

Technical Editor: Francis H.R. Franca.

✉ R. M. Cotta
  cotta@mecanica.coppe.ufrj.br

[1] Interdisciplinary Nucleus of Fluid Dynamics – NIDF, Laboratory of Transmission and Technology of Heat – LTTC, Department of Mechanical Engineering, PEM/COPPE/UFRJ - Universidade Federal do Rio de Janeiro, Cx. Postal 68503, Rio de Janeiro, RJ CEP 21945-970, Brazil

[2] ATS4i Aero-Thermal Solutions for Industry, São Paulo, Brazil

🗷 Springer

1490

J Braz. Soc. Mech. Sci. Eng. (2016) 38:1489–1509

1 Introduction

Conjugated problems are essential in predicting heat transfer rates and heat transfer coefficients for most applications in thermal engineering when accuracy is at a premium, and when the simplifying assumptions that allow for the decoupling of the two heat transfer modes, convection and conduction, at the fluid streams and participating walls, respectively, are no longer applicable. The analytical treatment of conjugated problems is one of the classical contributions of Luikov and collaborators [1, 2], who consolidated the physical interpretation and first analytical predictions of conjugated heat transfer, after the pioneering work of Perelman [3]. Following their work, it became possible to verify, and eventually avoid, approximate solutions based on simplified pure convection formulations, when the wall is considered not to undergo a relevant heat conduction process, or on pure conduction formulations, when the fluid convection is accounted for in the form of heat transfer coefficient correlations for idealized boundary conditions, in general as prescribed temperatures or heat fluxes.

Nevertheless, the analytical treatment of such class of conjugated problems has inherent mathematical difficulties due to the coupled partial differential system of energy balance equations for the interacting solid and fluid regions. The Generalized Integral Transform Technique (GITT) [4–8] has been employed in the hybrid numerical–analytical solution of conjugated problems, both in the context of internal and external flow applications [9–16]. Recently [12–16], the idea of a single-domain reformulation of the conjugated problem has been introduced, which allows for the representation of the energy equations in all involved solid and fluid regions as a single one, with space variable coefficients having abrupt transitions at the interfaces, which significantly simplifies the integral transformation process and provides a systematic approach for complex configurations and irregular regions [17, 18]. In parallel, the GITT approach was consolidated into a general purpose open source code named UNIT (Unified Integral Transforms) [19–22] written in the symbolic computation platform *Mathematica* [23], for disseminating its use among researchers motivated by analytic-based simulation.

Aeronautical thermal protection systems must be designed so that the solid structure is capable of rapidly responding to the external convective stimulus, due to sudden variations of atmospheric and flight conditions, being thus essential to solve a conjugated conduction–convection problem in such cases. Ignoring this mutual influence could lead to erroneous results and physical conclusions that would induce the designer to a non-conservative conception. Icing of aeronautical surfaces and the consequent degradation in flight performance under high altitude and adverse atmospheric conditions is a well-known phenomenon even before World War II. The main affected parts are the wings, empennages, engine intakes, frontal cone, landing gear compartment's door and sensors [24, 25]. Among these, the case of the Pitot tube is emphasized in this work since it is still a fundamental equipment for guidance and navigation of modern aeronautical systems. The icing of such probes can generate unreliable local velocity readings and compromise the flight control. The catastrophic effects of this kind of failure can be observed when analyzing the fairly recent accident that occurred with the AF447 flight in 2009, in which the Pitot probes icing, complicated by deficient crew training in high altitude flights with abrupt loss of lift, was pointed out as the main cause of the disaster by the investigations conducted by the Bureau d'Enquêtes et d'Analyses pour la Sécurité de l'Aviation Civile (BEA), in France. However, this was not the only accident in which the icing of the sensors was pointed out as the main cause of an aeronautical disaster. In a brief survey conducted, a number of cases were found with very similar circumstances as that of the AF447, showing the importance of pursuing further analysis on the subject.

The present work provides a review of the theoretical–experimental research undertaken at the Interdisciplinary Nucleus of Fluid Dynamics, NIDF/COPPE-UFRJ, since the AF447 tragedy, on the thermal analysis of Pitot tubes with anti-icing systems. In a series of fairly recent contributions [26–32], the conjugated heat transfer analysis of heated Pitot tubes and wing sections was modeled and solved through the GITT, together with a well-accepted ice accretion model and algorithm, and experimentally validated with actual flight tests and wind tunnel experiments. This review work has the objective of consolidating such recent developments towards advancing analytical tools for understanding anti-icing systems for aeronautical velocity sensors and structures, through the formulation of the required conjugated conduction–convection problem and the adoption of robust hybrid numerical–analytical solution methodologies. The analysis of the thermal behavior that precedes the onset of ice formation, as well as the ice accretion process itself, can be used to modify the probe design, aimed at avoiding the freezing of the impinging supercooled droplets and at improving de-icing behavior under critical situations.

2 Solution methodology

Various classes of linear and nonlinear convection–diffusion problems can be handled by the formal integral transforms procedure, known as GITT (Generalized integral transforms technique) [4–8] and widely available as the UNIT code [19–22] in the *Mathematica* platform. In order

to offer an unified view, a transient convection–diffusion problem of n coupled potentials is considered, defined in region V, with boundary surface S and including nonlinear coefficients and convective terms, incorporated into the source terms, as follows:

$$w_k(\mathbf{x})L_{k,t}T_k(\mathbf{x},t) = G_k(\mathbf{x},t,\mathbf{T}), \quad \mathbf{x} \in V, t > 0, k = 1, 2, \ldots, n, \tag{1a}$$

where the t operator, $L_{k,t}$, for a parabolic or parabolic-hyperbolic formulation is given by

$$L_{k,t} \equiv \frac{\partial}{\partial t} \tag{1b}$$

and

$$G_k(\mathbf{x},t,\mathbf{T}) = \nabla \cdot (K_k(\mathbf{x})\nabla T_k(\mathbf{x},t)) - d_k(\mathbf{x})T_k(\mathbf{x},t) + g_k(\mathbf{x},t,\mathbf{T}) \tag{1c}$$

with initial and boundary conditions given, respectively, by

$$T_k(\mathbf{x},0) = f_k(\mathbf{x}), \quad \mathbf{x} \in V \tag{1d}$$

$$\left[\alpha_k(\mathbf{x}) + \beta_k(\mathbf{x})K_k(\mathbf{x})\frac{\partial}{\partial \mathbf{n}}\right]T_k(\mathbf{x},t) = \phi_k(\mathbf{x},t,\mathbf{T}), \quad \mathbf{x} \in S, t > 0, \tag{1e}$$

where $\mathbf{n}$ denotes the outward-drawn normal to the surface S, and where the potentials vector is given by

$$\mathbf{T} = \{T_1, T_2, \ldots, T_k, \ldots, T_n\}^T \tag{1f}$$

Equations (1) are sufficiently general once all nonlinear and convection terms are grouped within the equations and boundaries source terms. For linear source terms, i.e., $g \equiv g(\mathbf{x},t)$, and $\phi \equiv \phi(\mathbf{x},t)$, exact analytical solutions are readily available via the Classical Integral Transform Technique [33]. Otherwise, this problem is not exactly transformable, and the ideas in the Generalized Integral Transform Technique [4–8] can be utilized to develop hybrid numerical–analytical solutions, as summarized below.

The formal integral transform solution requires the proposition of eigenfunction expansions for the associated potentials. The linear situation mentioned above naturally leads to the eigenvalue problems to be preferred in the analysis of the nonlinear situation as well. They appear in the direct application of the separation of variables methodology to the linear homogeneous version of the proposed problem. Thus, the recommended set of uncoupled auxiliary problems is given by

$$\nabla \cdot (K_k(\mathbf{x})\nabla \psi_{ki}(\mathbf{x})) + \left[\mu_{ki}^2 w_k(\mathbf{x}) - d_k(\mathbf{x})\right]\psi_{ki}(\mathbf{x}) = 0, \quad \mathbf{x} \in V \tag{2a}$$

$$\left[\alpha_k(\mathbf{x}) + \beta_k(\mathbf{x})K_k(\mathbf{x})\frac{\partial}{\partial \mathbf{n}}\right]\psi_{ki}(\mathbf{x}) = 0, \quad \mathbf{x} \in S, \tag{2b}$$

where the eigenvalues, μ_{ki}, and related eigenfunctions, $\psi_{ki}(\mathbf{x})$, are assumed to be known from exact analytical

expressions obtainable through symbolic computation systems [23] or application of computational methods for Sturm–Liouville type problems [5]. In fact, Eqs. (1) already reflect this choice of eigenvalue problems, Eqs. (2), via prescription of the linear coefficients in both the equations and boundary conditions, since any remaining term is directly incorporated into the general nonlinear source terms without loss of generality. Equations (2) allow, through the orthogonality property of the eigenfunctions, the definition of the integral transform pairs:

$$\bar{T}_{ki}(t) = \int_V w_k(\mathbf{x})\tilde{\psi}_{ki}(\mathbf{x})T_k(\mathbf{x},t)dv, \quad \text{transforms} \tag{3a}$$

$$T_k(\mathbf{x},t) = \sum_{i=1}^{\infty}\tilde{\psi}_{ki}(\mathbf{x})\bar{T}_{k,i}(t), \quad \text{inverses,} \tag{3b}$$

where the symmetric kernels $\tilde{\psi}_{ki}(\mathbf{x})$ are given by

$$\tilde{\psi}_{ki}(\mathbf{x}) = \frac{\psi_{ki}(\mathbf{x})}{\sqrt{N_{ki}}}; N_{ki} = \int_v w_k(\mathbf{x})\psi_{ki}^2(\mathbf{x})dv \tag{3c, d}$$

with N_{ki} being the normalization integrals.

The integral transformation of Eq. (1a) is accomplished by applying the operator $\int_V \tilde{\psi}_{ki}(\mathbf{x})(\cdot)dv$ and making use of the boundary conditions given by Eqs. (1d) and (2b), yielding

$$\frac{d\bar{T}_{ki}(t)}{dt} + \mu_{ki}^2\bar{T}_{ki}(t) = \bar{g}_{ki}(t,\mathbf{T}) + \bar{b}_{ki}(t,\mathbf{T}),$$
$$i = 1, 2, \ldots, t > 0, k = 1, 2, \ldots, n, \tag{4a}$$

where the transformed source term $\bar{g}_{ki}(t,\mathbf{T})$ is due to the integral transformation of the equation source term, and the other, $\bar{b}_{ki}(t,\mathbf{T})$, is due to the contribution of the boundary source term:

$$\bar{g}_{ki}(t,\mathbf{T}) = \int_v \tilde{\psi}_{ki}(\mathbf{x})g_k(\mathbf{x},t,\mathbf{T})dv;$$
$$\bar{b}_{ki}(t,\mathbf{T}) = \int_S K_k(\mathbf{x})\left[\tilde{\psi}_{ki}(\mathbf{x})\frac{\partial T_k(\mathbf{x},t)}{\partial \mathbf{n}} - T_k(\mathbf{x},t)\frac{\partial \tilde{\psi}_{ki}(\mathbf{x})}{\partial \mathbf{n}}\right]ds \tag{4b}$$

The boundary conditions contribution may also be expressed in terms of the boundary source terms, after manipulating Eqs. (1d) and (2b), to yield

$$\bar{b}_{ki}(t,\mathbf{T}) = \int_S \phi_k(\mathbf{x},t,\mathbf{T})\left[\frac{\tilde{\psi}_{ki}(\mathbf{x}) - K_k(\mathbf{x})\frac{\partial \tilde{\psi}_{ki}(\mathbf{x})}{\partial \mathbf{n}}}{\alpha_k(\mathbf{x}) + \beta_k(\mathbf{x})}\right]ds \tag{4c}$$

The initial conditions given by Eq. (1c) are also transformed to provide

$$\bar{T}_{ki}(0) = \bar{f}_{ki} \equiv \int_v w_k(\mathbf{x})\tilde{\psi}_{ki}(\mathbf{x})f_k(\mathbf{x})dv \tag{4d}$$

1492

J Braz. Soc. Mech. Sci. Eng. (2016) 38:1489–1509

Equations (4) form an infinite coupled system of nonlinear ordinary differential equations for the transformed potentials, $\bar{T}_{k,i}(t)$, which is unlikely to be analytically solvable. Nevertheless, reliable algorithms are readily available to numerically handle this ODE system, after truncation to a sufficiently large finite order. The *Mathematica* system [23] provides the routine *NDSolve* for solving stiff ODE systems such as the one here obtained, under automatic absolute and relative error control. Once the transformed potentials have been numerically computed, the *Mathematica* routine automatically provides an interpolating function object that approximates the *t* variable behavior of the solution in a continuous form. Then, the inversion formula can be recalled to yield the potential field representation at any desired position **x** and time *t* (or equivalent space coordinate).

The formal solution above reviewed provides the basic working expressions for the integral transform method (GITT). However, for an improved computational performance, it is always recommended to reduce the importance of the equation and boundary source terms so as to enhance the eigenfunction expansions convergence behavior [6]. The UNIT code for multidimensional applications allows for user provided filters, which depend on the user's experience, but it is also implemented an automatic progressive linear filtering option [22]. The constructed multidimensional UNIT code in the *Mathematica* platform [21, 22] encompasses all of the symbolic derivations that are required in the above GITT formal solution, besides the numerical computations that are required in the solutions of the chosen eigenvalue problems and the transformed differential system.

An alternative solution strategy to the total integral transformation described above is of particular interest in the treatment of transient convection–diffusion problems with a preferential convective direction [22], which has also been explored in the realm of the present project. In such cases, the partial integral transformation of the original system, in all but one space coordinate, may offer an interesting combination of relative advantages between the eigenfunction expansion approach and the selected numerical method for handling the coupled system of one-dimensional partial differential equations that result from the partial transformation procedure.

It is also of interest in the present context, to briefly describe the single-domain reformulation strategy for solving convection–diffusion problems in complex configurations and irregular regions, recently introduced in the context of conjugated problems [9–16]. Consider now that the general transient diffusion or convection–diffusion problem
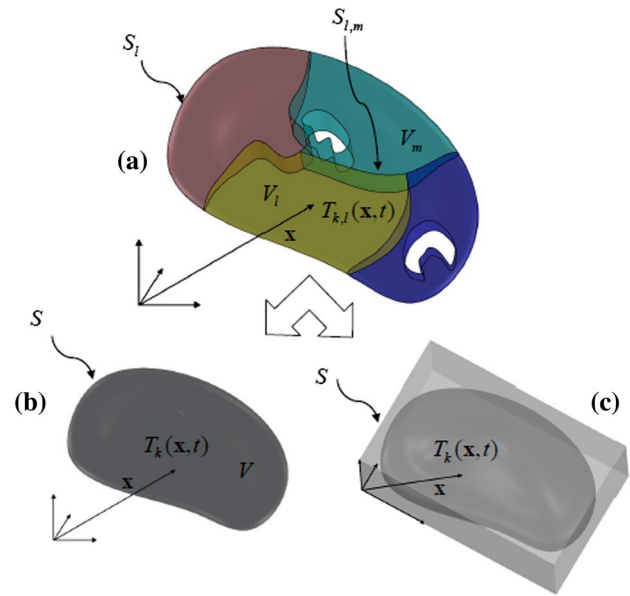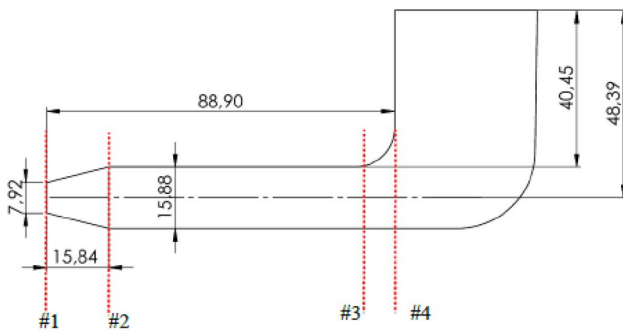

Fig. 1 a Diffusion or convection–diffusion in a complex multidimensional configuration with n_V sub-regions. **b** Single-domain representation keeping the original overall domain. **c** Single-domain representation considering a regular overall domain that envelopes the original one

of Eq. (1) is defined in a complex multidimensional configuration that is represented by n_V different sub-regions with volumes V_l, $l = 1, 2, \ldots, n_V$, with potential and flux continuity at the interfaces among themselves, as illustrated in Fig. 1a. We consider that a certain number of potentials are to be calculated in each sub-region, $T_{k,l}(\mathbf{x}, t)$, $k = 1, 2, \ldots, n$, governed in the corresponding sub-region through a fairly general formulation, such as in Eq. (1), with appropriate interface and boundary conditions, respectively at the interfaces, $S_{l,m}$, and external surfaces, S_l. The integral transform method can be applied to solve this more involved system of equations, either by constructing an individual eigenfunction expansion basis for each potential, and then coupling all the transformed systems and potentials for each sub-region, or by constructing a multiregion eigenvalue problem that couples all of the sub-regions into a single set of eigenvalues, which in general involves cumbersome computations in multidimensional applications. However, in this case, one single-transformed system and one single set of transformed potentials are obtained by employing the appropriate orthogonality property.

Figure 1a–c provide two possibilities for representation of the single domain, either by keeping the original overall domain after definition of the space variable coefficients, as shown in Fig. 1b, or, if desired, by considering
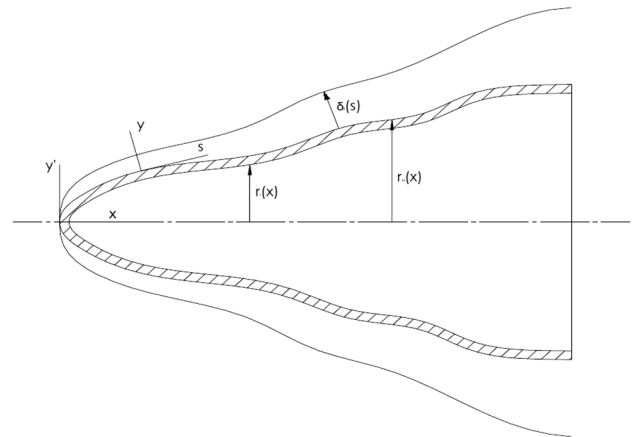
(a)

(b)

Fig. 2 **a** Pitot probe PH-510 used as the basis for the proposed thermal model. **b** Schematic drawing of the Pitot tube with main dimensions (mm)

Fig. 3 Coordinates system for the axissymetrical configuration of a sensor with arbitrary geometry and its interaction with the external boundary layer

3 Direct problem formulation

In light of the opportunity offered by the Brazilian Navy in performing tests with their A-4 Skyhawk aircrafts, the Pitot tube model PH510 by Aero-Instruments, Co., shown in Fig. 2a, and with its main dimensions in Fig. 2b, was used as the basis for the modeling here developed, having essentially the same characteristics of modern velocity probes for commercial flights. It is important to mention that the Pitot tube in consideration is equipped with an anti-icing thermal protection system located in the central cylindrical part of its body (region between lines #2 and #3 in Fig. 2b), which consists of a resistive metallic wire embedded in a ceramic electrical insulation. From the stagnation region at the conical tip until close to the leading edge of the support, which resembles a wing, where the heated region ends, the material used is copper (region between lines #1 and #3), while the rest is made of brass (after line #3 to the end of the support). The exception is the electrical insulation present in the heated region that is composed of porcelain which will be the subject of further discussions in what follows. The detailed knowledge of the flow and heat transfer processes over and along the probe itself is essential for its thermal management, specially near the stagnation region due to its functional importance, while the wing-like support region holds little importance to the thermal behavior of the sensor as a whole [26].

Aiming at developing a thermal model for the Pitot probe with anti-icing system, two physical regions are considered. The first one is the solid shell that comprises the

a regular overall domain that envelopes the original one, as shown in Fig. 1c. Irregular domains can be directly integral transformed [5, 8] and, in principle, there is no need to consider the second representation possibility pointed out above. However, some computational advantages in some cases may be achieved by enveloping the original irregular domain by a simple regular region, especially in the context of automatic solution procedures, such as when using the UNIT algorithm and code [21, 22], discussed above.

Therefore, as already demonstrated in the analysis of specific conjugated problems [12–16], it is possible to rewrite the multiregion problem as a single-domain formulation with space variable coefficients and source terms. Such space variable coefficients then incorporate the abrupt transitions among the different sub-regions and permit the complex configuration representation as a single-domain formulation, such as in Eq. (1a), to be directly handled by integral transforms.

1494

J Braz. Soc. Mech. Sci. Eng. (2016) 38:1489–1509

body of the sensor which is modeled through the heat conduction equation with an energy generation term, due to the anti-icing heating. The other region is related to the velocity and thermal boundary layers that are formed around the axisymmetric shape of the sensor, as depicted in general form in Fig. 3 below. The boundary layers are then considered in two regions, laminar and turbulent, that are treated sequentially and, at the first modeling effort, with a sharp transition when the critical Reynolds number is reached. The flow external to the boundary layer is also required, where the influence of the viscosity is not relevant and an inviscid model can be invoked. Moreover, there are analytical relations for the potential flow over an axisymmetric body that are readily available from classical aerodynamics texts, due to its importance in calculations of fuselage bodies. With the velocity field and making the assumption that the flow is isentropic, the temperature, density and dynamical viscosity fields, using the Sutherland relation, easily follow [34]. The relations chosen in the present work are derived from [35], which is based on sources and sink distributions to establish the velocity fields at the border of the boundary layer, a common approach in potential flow theory. However, the originally proposed equations apply strictly only to incompressible flows, but correction factors were developed in order to take advantage of the simplicity of such results. Here, the Prandtl–Glauert correction is adopted since, even though there are more accurate factors, it is explicit, straightforward, and sufficiently precise for our purposes. The interaction between the solid and fluid regions occurs through the continuity relations for the temperature field and heat flux at the solid–fluid interface.

The geometrical complexity of the probe initially posed difficulties in formulating a simplified model to the whole extension of the Pitot tube. However, a detailed local reproduction of the temperature field at the wing-shaped support of the probe is not relevant, as observed in previous works [26, 27], which allows simplification of the curvature effects in the transition from the conical–cylindrical portion towards the junction with the support. The mathematical model for heat conduction along the considered axisymmetric Pitot tube is presented in Eq. (5a–f), employing cylindrical coordinates.

$$w(x,r)\frac{\partial T_s}{\partial t} = \frac{\partial}{\partial x}\left(k(x,r)\frac{\partial T_s}{\partial x}\right) + \frac{1}{r}\frac{\partial}{\partial r}\left(k(x,r)r\frac{\partial T_s}{\partial r}\right) + g(x,r,t),$$
$$0 \le x \le L,\ r_i(x) \le r \le r_o(x) \tag{5a}$$

$$T_s(x,r,0) = T_0(x,r) \tag{5b}$$

$$h_e T_s(0,r,t) - k(0,r)\left.\frac{\partial T_s}{\partial x}\right|_{x=0} = h_e T_{aw}; \quad \left.\frac{\partial T_s}{\partial x}\right|_{x=L} = 0 \tag{5c, d}$$

$$\left.\frac{\partial T_s}{\partial \boldsymbol{n}}\right|_{r=r_i(x)} = 0; \quad h(x)T_s(x,r_o(x),t) + k(x)\left.\frac{\partial T_s}{\partial \boldsymbol{n}}\right|_{r=r_o(x)} = h(x)T_{aw} \tag{5e, f}$$

In the above formulation, heat transfer from the probe support to the airplane structure is neglected, due to the minor importance of this region in the desired thermal analysis [26]. Also, Newton's law of cooling at the boundary conditions is written for a more general conjugated problem with compressible flow, and for this reason, the adiabatic wall temperature becomes important to the proposition of a model applicable in the whole envelope of applications desired.

Knowing that metallic materials are predominant in the sensor structure and that the wall thicknesses are in general small, it is expected that the Biot numbers are sufficiently low allowing for the application of a lumping procedure in the radial direction, towards the simplification of the solid heat conduction model. Both the classical lumped and the improved lumped approaches [6] were considered in the present context and a comparison between the two approaches has also been conducted. The so-called Coupled Integral Equations Approach (CIEA) [6] for reformulation of differential problems is based on the proposition of approximations for both the averaged potential and its gradient as a function of the average potential, as defined through the integration in one or more spatial variables. For our specific problem, the radially averaged temperature is defined as

$$T_{av}(x,t) = \frac{2}{r_o^2 - r_i^2}\int_{r_i(x)}^{r_o(x)} T_s(x,r,t)r\,\mathrm{d}r \tag{6}$$

Applying the same averaging operator in the differential model under analysis, it is possible to make use of Hermite approximations for numerical integration and to reformulate the transient two-dimensional model (5a–f) into a transient one-dimensional model [6]. Thus, applying the averaging operator in the radial direction to Eq. (5a), using the definition of the radially averaged temperature, Eq. (6), and considering that the variation of the transversal section area with the longitudinal direction is mild, so as to approximate the normal derivatives by radial ones, it is possible to rewrite the partial differential model of Eq. (5a–f) as

$$w_{av}(x)\frac{\partial T_{av}}{\partial t} = \frac{1}{A(x)}\frac{\partial}{\partial x}\left(k_{av}(x)A(x)\frac{\partial T_{av}}{\partial x}\right) + \frac{2k_{av}(x)r_o}{r_o^2 - r_i^2}\left.\frac{\partial T_s}{\partial r}\right|_{r=r_o(x)}$$
$$+ g_{av}(x,t), \quad 0 \le x \le L \tag{7a}$$

$$T_{av}(x,0) = T_{av0}(x) \tag{7b}$$

$$h_e T_{av}(0,t) - k_{av}(0)\left.\frac{\partial T_{av}}{\partial x}\right|_{x=0} = h_e T_{aw}; \quad \left.\frac{\partial T_{av}}{\partial x}\right|_{x=L} = 0 \tag{7c, d}$$

Using Hermite approximations to numerically integrate Eq. (6) and the known integral of the gradient over the domain, together with the boundary conditions in the radial direction, it is possible to relate the local term in Eq. (7a) that is evaluated at the surface of the probe, with the average temperature, which results in Eq. (8a–c), consisting of the so-called improved lumped approach [6]:

$$h_e T_{av}(0,t) - k_{av}(0) \left.\frac{\partial T_{av}}{\partial x}\right|_{x=0} = h_e T_{aw}; \quad \left.\frac{\partial T_{av}}{\partial x}\right|_{x=L} = 0 \tag{10e, f}$$

The probe materials and radial dimensions vary with the longitudinal direction, and these changes in the effective thermophysical properties and transversal section are very

$$T_s(x, r_i, t) = \frac{12 k_{av}(x)(r_o + r_i) T_{av}(x,t) + h(x)(r_o - r_i)[6(r_o + r_i) T_{av}(x,t) - (3r_o + r_i) T_{aw}]}{12 k_{av}(x)(r_o + r_i) + h(x)(3r_o + 5r_i)(r_o - r_i)} \tag{8a}$$

$$T_s(x, r_o, t) = T_{aw} + \frac{12 k_{av}(x)(r_o + r_i)(T_{av}(x,t) - T_{aw})}{12 k_{av}(x)(r_o + r_i) + h(x)(3r_o + 5r_i)(r_o - r_i)} \tag{8b}$$

$$\left.\frac{\partial T_s}{\partial r}\right|_{r=r_o(x)} = -\frac{12 h(x)(r_o + r_i)(T_{av}(x,t) - T_{aw})}{12 k_{av}(x)(r_o + r_i) + h(x)(3r_o + 5r_i)(r_o - r_i)} \tag{8c}$$

For the classical lumped analysis, the temperature of the surface is simply approximated by the average temperature in the boundary condition (5f), also allowing for the association of the local term in the right-hand side of Eq. (7a) with the average temperature. In this case, the local temperatures at the internal and external surfaces of the probe, and the boundary condition at the external surface, are approximated as in Eq. (9a–c):

$$T_s(x, r_o, t) \cong T_s(x, r_i, t) \cong T_{av}(x,t) \tag{9a, b}$$

$$\left.\frac{\partial T_s}{\partial r}\right|_{r=r_o(x)} \cong \frac{h(x)}{k_{av}(x)}(T_{aw} - T_{av}(x,t)) \tag{9c}$$

Equation (7a–c) are in fact directly applicable only to the axisymmetric portion of the Pitot probe, within $0 \leq x \leq a$, from the tip to line #4 in Fig. 2b. However, for the wing-like support, the use of the classical lumped approach is more easily applicable and sufficiently accurate for the present purposes. Therefore, as discussed above, neglecting the curvature effects on heat transfer to the support region, $a \leq x \leq L$, the complete improved lumped model for the Pitot probe becomes

$$w_{av}(x)\frac{\partial T_{av}}{\partial t} = \frac{1}{A(x)}\frac{\partial}{\partial x}\left(k_{av}(x)A(x)\frac{\partial T_{av}}{\partial x}\right) \tag{10a}$$
$$- \Omega(x)(T_{av}(x,t) - T_{aw}) + g_{av}(x,t)$$

$$\Omega(x) = \begin{cases} \frac{24 h(x) k_{av}(x) r_o}{12 k_{av}(x)(r_o^2 - r_i^2) + h(x)(r_o - r_i)^2(3r_o + 5r_i)}, & 0 \leq x \leq a \\ \frac{h(x)P(x)}{A(x)}, & a \leq x \leq L \end{cases} \tag{10b, c}$$

$$T_{av}(x, 0) = T_{av0}(x) \tag{10d}$$

important to the model response. It should be noted that there is a sharp step in the thermal capacity at the end of the cone portion of the probe, that is 16 mm apart from the stagnation point. This is due to the large heat capacity of the ceramic material used to electrically insulate the resistance from the probe along the heated portion. On the other hand, the influence of this ceramic material in the effective thermal conductivity is less significant, as expected, since it has thermal insulating properties.

The coupling of the heat conduction problem along the probe with the fluid flow over its body was initially investigated through the use of appropriate correlations for the heat transfer coefficients [26], at the stagnation point, along the probe length, and over the wing-like support. Afterwards, the actual conjugated problem was tackled, by simultaneously solving the probe energy equation and the fluid flow and energy equations [27–30]. The solution of the flow and energy equations in the fluid is carried only in the axisymmetric part of the Pitot tube allowing for the use of a specific coordinates system for this case. The flow is considered to be compressible, since it is desirable to cover all the flight envelope of modern commercial aircraft. As for the transient response, it was shown [27] that the time necessary for the flow to reach steady state is markedly less than that necessary for the solid to reach the same regime. Therefore, only the quasi-steady-state solution for the fluid needs to be considered here.

Within the limits of the boundary layer theory and from the assumptions that the fluid is Newtonian, that the Boussinesq postulate holds, and that the turbulent Prandtl number is constant [34], Eq. (11a–h) for the fluid flow problem were considered. For the sake of brevity, they are written in the form of Reynolds-averaged equations, and for laminar flow, the turbulent properties are set to zero.

$$\bar{\rho}\bar{u}\frac{\partial \bar{u}}{\partial s} + \bar{\rho}\bar{v}\frac{\partial \bar{u}}{\partial y} = \rho_e u_e \frac{du_e}{ds} + \frac{1}{r}\frac{\partial}{\partial y}\left[(\mu + \mu_t)r\frac{\partial \bar{u}}{\partial y}\right] \tag{11a}$$

$$\bar{u}(0) = 0, \bar{u}(\infty) = u_e, \left.\frac{\partial \bar{u}}{\partial y}\right|_{y=\infty} = 0 \tag{11b–d}$$

1496

J Braz. Soc. Mech. Sci. Eng. (2016) 38:1489–1509

$$\bar{\rho}\bar{u}\frac{\partial \bar{H}}{\partial s} + \overline{\rho v}\frac{\partial \bar{H}}{\partial y} = \frac{1}{r}\frac{\partial}{\partial y}\left[\left(\frac{\mu}{Pr} + \frac{\mu_t}{Pr_t}\right)r\frac{\partial \bar{H}}{\partial y}\right]$$
$$+ \frac{1}{r}\frac{\partial}{\partial y}\left[\mu r\left(1 - \frac{1}{Pr}\right) + \mu_t r\left(1 - \frac{1}{Pr_t}\right)\right]\frac{\partial}{\partial y}\left(\frac{\bar{u}^2}{2}\right)$$
(11e)

$$\bar{H}(0) = c_p T_w, \quad \bar{H}(\infty) = H_e, \quad \left.\frac{\partial \bar{H}}{\partial y}\right|_{y=\infty} = 0 \qquad (11\text{f–h})$$

The governing equations for determining the ice accretion rates were implemented using the extended Messinger model [36–38]. At low temperatures and low liquid water contents, rime ice occurs, for which the ice shape is determined by a simple mass balance. At warmer temperatures and high liquid water contents, glaze ice forms, for which the energy and mass conservation equations are solved numerically. Once the ice and liquid water film thicknesses are obtained, the water height and the temperatures in the different layers may be calculated, through a quasi-steady one-dimensional heat conduction model. The mass and energy balances employed in the analysis of ice accretion over wings can be directly applied to the study of ice formation on Pitot probes. However, the heat transfer by convection and the latent heat are the most important terms in the energy balance, as discussed in [31].

More recently [39], a fully local differential formulation was considered, adopting the single-domain formulation strategy, to the solution of the conjugated conduction–convection problem as applied to the analysis of wing sections under ice formation conditions, which can be readily extended to the analysis of axisymmetric sensors. Figure 4 illustrates the representation of the single domain and the associated coordinates system.

The solid and fluid energy equations are then given, respectively, by Eqs. (12) and (13) below, with the corresponding boundary conditions:

$$k_{\text{sol}}\left(\frac{\partial^2 T_1}{\partial s^2} + \frac{\partial^2 T_1}{\partial z^2}\right) + G(s,z) = 0 \qquad (12\text{a})$$

$$\left.\frac{\partial T_1}{\partial s}\right|_{s=0} = 0; \qquad \left.\frac{\partial T_1}{\partial s}\right|_{s=L} = 0 \qquad (12\text{b, c})$$

$$-k_{\text{sol}}\left.\frac{\partial T_1}{\partial z}\right|_{z=0} = q_w; \qquad -k_{\text{sol}}\left.\frac{\partial T_1}{\partial z}\right|_{z=\varepsilon} = -k_f\left.\frac{\partial T_2}{\partial z}\right|_{z=\varepsilon}$$
(12d, e)

$$w_f u(s,z)\frac{\partial T_2}{\partial s} + w_f v(s,z)\frac{\partial T_2}{\partial z} = k_f\left(\frac{\partial^2 T_2}{\partial s^2} + \frac{\partial^2 T_2}{\partial z^2}\right) + w_f\frac{\partial}{\partial z}\left[\frac{l^2}{Pr_t}\frac{\partial u}{\partial z}\frac{\partial T_2}{\partial z}\right]$$
(13a)

$$\left.\frac{\partial T_2}{\partial s}\right|_{s=0} = 0; \qquad \left.\frac{\partial T_2}{\partial s}\right|_{s=L} = 0 \qquad (13\text{b, c})$$
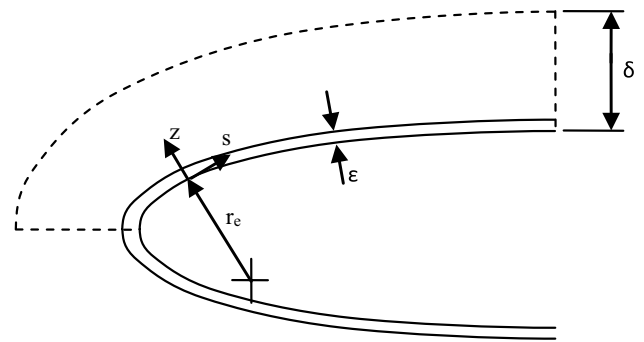
Fig. 4 Single-domain representation for conjugated problem analysis of wing sections

$$T_1(s,\varepsilon) = T_2(s,\varepsilon); \qquad T(s,\delta) = T_\infty \qquad (13\text{d, e})$$

However, in terms of the single-domain representation, these equations are merged into the single system represented by Eqs. (14) below, where the z variable coefficients incorporate the abrupt transition between the two subregions, as previously discussed.

$$w_f u(s,z)\frac{\partial T}{\partial s} + w_f v(s,z)\frac{\partial T}{\partial z} = k(z)\frac{\partial^2 T}{\partial s^2}$$
$$+ \frac{\partial}{\partial z}\left[k(z)\frac{\partial T}{\partial z}\right] + w_f\frac{\partial}{\partial z}\left[\frac{l^2}{Pr_t}\frac{\partial u}{\partial z}\frac{\partial T}{\partial z}\right] + G(s,z) \qquad (14\text{a})$$

$$\left.\frac{\partial T}{\partial s}\right|_{s=0} = 0; \qquad \left.\frac{\partial T}{\partial s}\right|_{s=L} = 0 \qquad (14\text{b, c})$$

$$-k_{\text{sol}}\left.\frac{\partial T}{\partial z}\right|_{z=0} = q_w; \qquad T(s,\delta) = T_\infty \qquad (14\text{d, e})$$

4 Inverse problem formulation

The objective of this section is to present the solution of an inverse heat conduction problem that complements the above theoretical analysis and aims at (1) estimating the heat transfer coefficient at the leading edge of Pitot tubes, in order to detect ice accretion; and (2) estimating the relative air speed in lack of reliable dynamic pressure readings. The main idea is to identify the relative air speed, by using transient temperature measurements of the Pitot tube at selected positions. It is thus an indirect measurement of the air speed through an inverse heat transfer analysis, which can be used to validate the speed measurement directly obtained through the Pitot tube. In addition, such indirect measurement may serve as a substitute for the Pitot tube readings in case of ice accretion, when the traditional sensor dynamic pressure

measurements become unreliable. Ice accretion at the tip of the Pitot tube is also identified through the estimation of the transient heat transfer coefficient $h_e(t)$, since it is then expected a sudden change in this heat transfer coefficient when ice accretion takes place, also as a result of the additional thermal resistance of the ice layer that is formed.

Due to the transient character of the present inverse problem, it is solved as a state estimation problem. In state estimation problems, the available measured data are used together with prior knowledge about the physical phenomena (formulation of the direct problem) and the measuring devices, in order to sequentially produce estimates of the desired dynamic variables. State estimation problems are solved with the so-called Bayesian filters, like the Kalman filter. The use of the Kalman filter is limited to linear models with additive Gaussian noises. On the other hand, Monte Carlo methods, usually denoted as particle filters, have been developed for cases that do not satisfy the restrictive hypotheses of the Kalman filter [40–46]. Its basic concept is to represent the required posterior density function by a set of random samples (particles) with associated weights, and to compute the estimates based on these samples and weights. As the number of samples becomes very large, this Monte Carlo characterization becomes an equivalent representation of the posterior probability function, and the solution approaches the optimal Bayesian estimate [40–46]. The mathematical model proposed by Souza et al. [28, 32] for the Pitot tube, as discussed above, is used in this analysis. The inverse problem is solved by using simulated transient temperature measurements at two different positions along the Pitot tube.

Let us consider the following state evolution model for the vector of state variables $\mathbf{x} \in R^{n_x}$ [40–46]:

$$\mathbf{x}_k = \mathbf{f}_k(\mathbf{x}_{k-1}, \mathbf{v}_{k-1}), \tag{15a}$$

where the subscript $k = 1, 2, \ldots$ denotes a time instant t_k in a dynamic problem and $\mathbf{f}$ is in general a non-linear function of the state variables $\mathbf{x}$ and of the state noise vector $\mathbf{v} \in R^{n_v}$. Consider also that measurements $\mathbf{z}_k \in R^{n_z}$ are available at t_k, $k = 1, 2, \ldots$. The measurements are related to the state variables $\mathbf{x}$ through the general function $\mathbf{h}$ in the observation (measurement) model:

$$\mathbf{z}_k = \mathbf{h}_k(\mathbf{x}_k, \mathbf{n}_k), \tag{15b}$$

where $\mathbf{n} \in R^{n_n}$ is the measurement noise.

The state estimation problem aims at obtaining information about $\mathbf{x}_k$ based on the state evolution model (15a) and on the measurements $\mathbf{z}_{1:k} = \{\mathbf{z}_i, i = 1, \ldots, k\}$ given by the observation model (15b) [40–46].

Let $\{\mathbf{x}_{0:k}^i, i = 0, \ldots, N\}$ be the particles with associated weights $\{w_k^i, i = 0, \ldots, N\}$ and $\mathbf{x}_{0:k} = \{\mathbf{x}_j, j = 0, \ldots, k\}$

be the set of all state variables up to t_k, where N is the number of particles. The weights are normalized so that $\sum_{i=1}^N w_k^i = 1$. Then, the marginal distribution of $\mathbf{x}_k$, which is of interest for the filtering problem, can be approximated by [43, 45]

$$\pi(\mathbf{x}_k | \mathbf{z}_{1:k}) \approx \sum_{i=1}^N w_k^i \, \delta\left(\mathbf{x}_k - \mathbf{x}_k^i\right) \tag{16}$$

The sequential application of the particle filter might result in the degeneracy phenomenon, where after a few states, all but very few particles have negligible weight [40–46]. The degeneracy implies that a large computational effort is devoted to updating particles whose contribution to the approximation of the posterior density function is almost zero. This problem can be overcome with a resampling step in the application of the particle filter. Resampling deals with the elimination of particles originally with low weights and the replication of particles with high weights. Resampling can be performed if the number of effective particles (particles with large weights) falls below a certain threshold number, but can also be applied indistinctively at every instant t_k, as in the Sampling Importance Resampling (SIR) algorithm described in [43, 45]. Such algorithm can be summarized in the steps presented in Table 1, as applied to the system evolution from t_{k-1} to t_k [43, 45].

In this work, the SIR algorithm is used for the estimation of the following state variables:

$$\mathbf{x}_k = \begin{bmatrix} \overline{\mathbf{T}}^k \\ h_e^k \\ u_\infty^k \end{bmatrix} = \begin{bmatrix} \bar{T}_0^k \\ \bar{T}_1^k \\ \vdots \\ \bar{T}_{NP-1}^k \\ \bar{T}_{NP}^k \\ h_e^k \\ u_\infty^k \end{bmatrix} \tag{17}$$

We note in Eq. (17) that, although the objective is the estimation of $h_e^k \equiv h_e(t_k)$ and $u_\infty^k \equiv u_\infty(t_k)$, due to the influence of these functions over the temperature field in the Pitot tube, the temperatures at the nodal points used for the discretization of the direct problem are also included in the vector of state variables. The state evolution model for the nodal temperatures in the Pitot tube is given by the discrete form of the direct problem [47]. The uncertainties for this model were taken as additive, Gaussian, with zero mean and a standard deviation of 1 % of the temperature value. Due to the lack of prior knowledge about the time evolutions of h_e^k and u_∞^k, but still aiming at specifying state evolution models with bounded variances for these

1498

J Braz. Soc. Mech. Sci. Eng. (2016) 38:1489–1509

Table 1 Sampling importance resampling algorithm [43, 45]

Step 1
For $i=1,\cdots,N$ draw new particles $\mathbf{x}_k^i$ from the prior density $\pi\left(\mathbf{x}_k\middle|\mathbf{x}_{k-1}^i\right)$ and then use the likelihood density to calculate the corresponding weights $w_k^i = \pi\left(\mathbf{z}_k\middle|\mathbf{x}_k^i\right)$.
Step 2
Calculate the total weight $T_w = \sum_{i=1}^{N} w_k^i$ and then normalize the particle weights, that is, for $i=1,\cdots,N$ let $w_k^i = T_w^{-1} w_k^i$
Step 3

Resample the particles as follows :
 	
 Construct the cumulative sum of weights (CSW) by computing $c_i = c_{i-1} + w_k^i$ for $i=1,\cdots,N$, with $c_0=0$.
 Let $i=1$ and draw a starting point u_1 from the uniform distribution $U\left[0, N^{-1}\right]$
 For $j=1,\cdots,N$
      Move along the CSW by making $u_j = u_1 + N^{-1}\left(j-1\right)$
      While $u_j > c_i$ make $i=i+1$.
      Assign sample $\mathbf{x}_k^j = \mathbf{x}_k^i$
      Assign sample $w_k^j = N^{-1}$

quantities, they were assumed to follow random walk models in the form:

$$u_\infty^k = u_\infty^{k-1}(1 + \sigma_u \varepsilon_u) \tag{18}$$

$$h_e^k = h_e^{k-1}(1 + \sigma_h \varepsilon_h), \tag{19}$$

where ε_u and ε_h are Gaussian random variables with zero means and unitary standard deviations, while σ_u and σ_h are the standard deviations of the random walk models for u_∞^k and h_e^k, respectively. Such standard deviations were taken as 0.05 and 0.2, respectively.

5 Experimental procedure

The first experimental results of the heated Pitot tube presented in this review were obtained in an aerodynamic wind tunnel at the Fluid Mechanics and Anemometry Division (DINAM), in the National Institute of Metrology, Standardization and Industrial Quality—INMETRO, Brazil, shown in Fig. 5 below. It is an open circuit blower-type tunnel and consists of a test section of 500 mm × 500 mm, 8-m long, and a 12.5 HP fan with variable speed control from 0 to 23 m/s. The main components of this experimental setup are the infrared camera FLIR SC660, a high-performance


Fig. 5 Open circuit blower-type wind tunnel of DINAM-INMETRO

infrared system with 640 × 480 image resolution used to obtain the temperature field at the Pitot surface, and the Particle Image Velocimetry (PIV) system, laser and camera, by DANTEC DYNAMICS, with a pulse duration of nanoseconds, wavelengths of 1064 and 532 nm with a laser medium of Nd:YAG. The Pitot probe was fixed to the floor of the wind tunnel through a PVC support, and in order to

Fig. 6 IR image of Pitot tube for an air flow free stream velocity of 10 m/s: **a** few seconds after the heater is turned on; **b** steady state
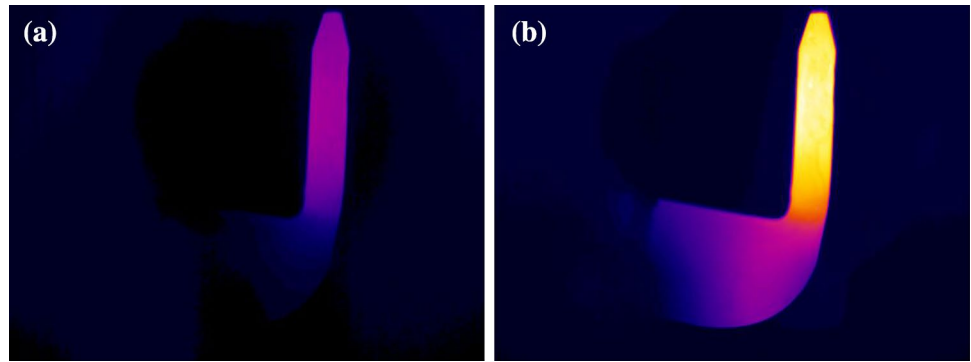
Fig. 7 **a** Pitot tube illuminated by laser during PIV test. **b** Average velocity field vector over upper Pitot tube surface calculated by PIV software ($u_\infty = 20$ m\s)
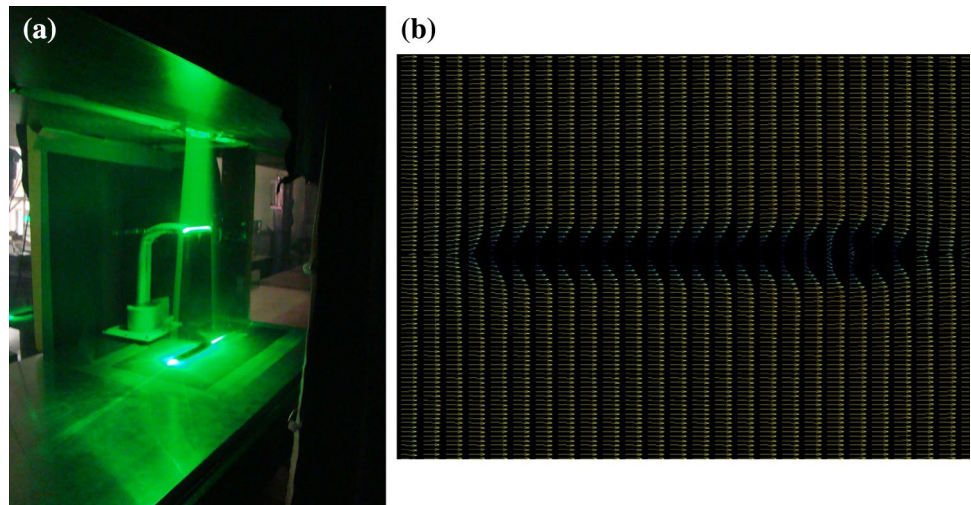
reduce uncertainty in the IR camera readings, its surface was painted with a graphite ink, which brought its emissivity to $\varepsilon = 0.97$, as stated by the ink manufacturer.

The experimental procedure was initiated by imposing a velocity to the wind tunnel test section, followed by the application of a voltage difference to the Pitot´s electrical resistance. Voltage and current are simultaneously measured along the experiment. Due to space limitations, the infrared thermography camera and laser source of the particle image velocimetry are not installed simultaneously, since both were required to be placed perpendicularly to the Pitot tube. Therefore, first, the infrared thermography measurements are taken along the transient process up to steady state, and then the PIV measurements are performed. For the IR images acquisition, the camera is connected to the acquisition computer by a fire-wire cable that makes it possible to achieve fast transfer of acquired data. Using the FLIR´s proprietary software, one can remotely operate the thermography camera, and monitor the temperature increase. Figure 6 illustrates the IR image produced by the FLIR SC660 camera of the heated Pitot tube in the beginning of the transient regime (Fig. 6a) and after the steady state is achieved (Fig. 6b). One may clearly observe

the temperature rise at the region of the Pitot heater and the temperature drop throughout the Pitot wing-shaped base.

Once steady state has been achieved, the IR camera is substituted by the laser source of the PIV system and the second phase of the experiment is initiated. The region to be studied is illuminated by the laser light plane. As tracer particles are dispersed in the fluid, a digital CCD camera, installed perpendicular to the laser plan, captures images from the illuminated particles. In Fig. 7a, one can observe the Pitot tube illuminated by a constant plane of laser during the PIV test and Fig. 7b illustrates the average velocity field vector calculated by the PIV software, showing the boundary layer at the Pitot upper surface, for 20 m/s dry air speed in the wind tunnel, confirming that the flow is mostly laminar over the conical–cylindrical region at such free stream velocities.

Next, experimental results for the transient thermal behavior of the heated Pitot tube were obtained from a A4-Skyhawk airplane of the VF-1 Squadron, in the Brazilian Aero-Naval Base, at São Pedro d´Aldeia, Rio de Janeiro, shown in Fig. 8. The A4 is a single seat, light weight, high-performance attack aircraft with a modified delta planform wing. It is powered by a Pratt and Whitney

Fig. 8 A4 Skyhawk airplane with tested Pitot probe

Fig. 9 Overall view of the climatic wind tunnel, NIDF, COPPE-UFRJ

gas turbine engine that produces a sea level static thrust of 11,200 pounds, making it possible to the aircraft to reach transonic speeds. The main components of this experimental analysis are the A-4 Pitot tube and the Testo Data Logger, model 177-T4. The data logger has four temperature channels which were used during the test flight, with type K thermocouples in a measuring rate of 3 s, and was switched on still on the ground, before the pilot powered the plane. The data logger was positioned in the front compartment of the plane, in a thermally insulated box. The thermocouples were fixed at increasing longitudinal distances from the tip of the Pitot tube, by a special glue made by Loctite, E-20NS Hysol Epoxy Adhesive, which is a long time curing, low viscosity structural adhesive.

During the flights, two redundant thermocouples were damaged, and thus, only the temperatures from the remaining two thermocouples were recorded along the whole test period. The thermocouple of major interest here was attached close to the end of the heated portion of the cylindrical body of the Pitot probe ($x = 80$ mm). The second recorded thermocouple was attached to the wing-shaped base of the Pitot probe, and its sensing tip was exposed to measure the external atmospheric temperature. The pilot was then responsible for promoting a transient thermal behavior on the Pitot tube, by turning the heating system off for a few seconds and then turning it on again, at different stable altitudes, for a few times in each altitude.

The final step in the experimental analysis then consisted of the design and construction of a climatic wind tunnel at COPPE/UFRJ [48], for future thermal analysis of the anti-icing system of the Pitot probe under conditions conducive to icing. The final testing of the climatic wind tunnel included the analysis of velocity fields along its test section and performing thermal experiments with the Pitot probe, similar to those reported in the previous experiments in the

wind tunnel of INMETRO. Figure 9 provides an overall picture of the climatic wind tunnel of NIDF-COPPE/UFRJ, designed to achieve Mach numbers around 0.3 at temperatures as low as −20 °C.

6 Results and discussion

6.1 Validation for incompressible flow: wind tunnel experiments

In [26], experiments were conducted in the metrological wind tunnel of INMETRO (Instituto Nacional de Metrologia, Padronização e Qualidade Industrial), in order to validate the simple heat conduction model then proposed for the Pitot probe, as well as the conjugated convection–conduction model for incompressible flow conditions. The measurements available include the LDA velocity field for the flow around the Pitot tube and the transient temperature distributions over the Pitot tube surface generated by infrared thermography, as illustrated in Fig. 10a. The model developed in [29] is here compared with the experimental results generated in [26]. Figure 10b shows the comparison between the steady-state results obtained with the simulation and the experiments, for the temperature distribution along the length of the probe, from the tip ($x = 0$) up to the end of the support region ($x = L$). Lines #2, 3, and 4 of Fig. 2b are also shown, to represent the heater region, between lines #2 and 3, and the beginning of the support, line #4. One may conclude that the adherence between the two sets of results is quite satisfactory, deviating only at the end of the support region, due to heat losses at the end of the Pitot tube support that were not accounted for by the model.

As for the transient behavior, starting from the unheated probe in thermal equilibrium with the free stream air, and suddenly turning on the heating system, the measurements taken by infrared thermography are compared in Fig. 11 with the simulation results for several positions along the
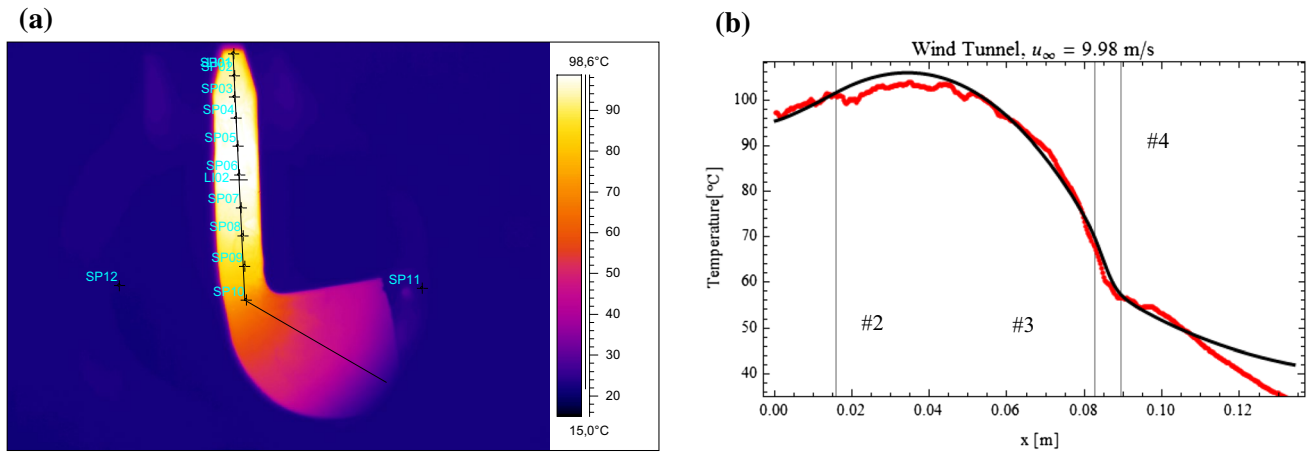
Fig. 10 a Illustration of the infrared thermography results from the wind tunnel experiments (9.98 m/s, 68 V and 0.69 A in the resistor). **b** Comparison between the steady-state temperature fields: experimental, in *red*, and simulated, in *black* (color figure online)
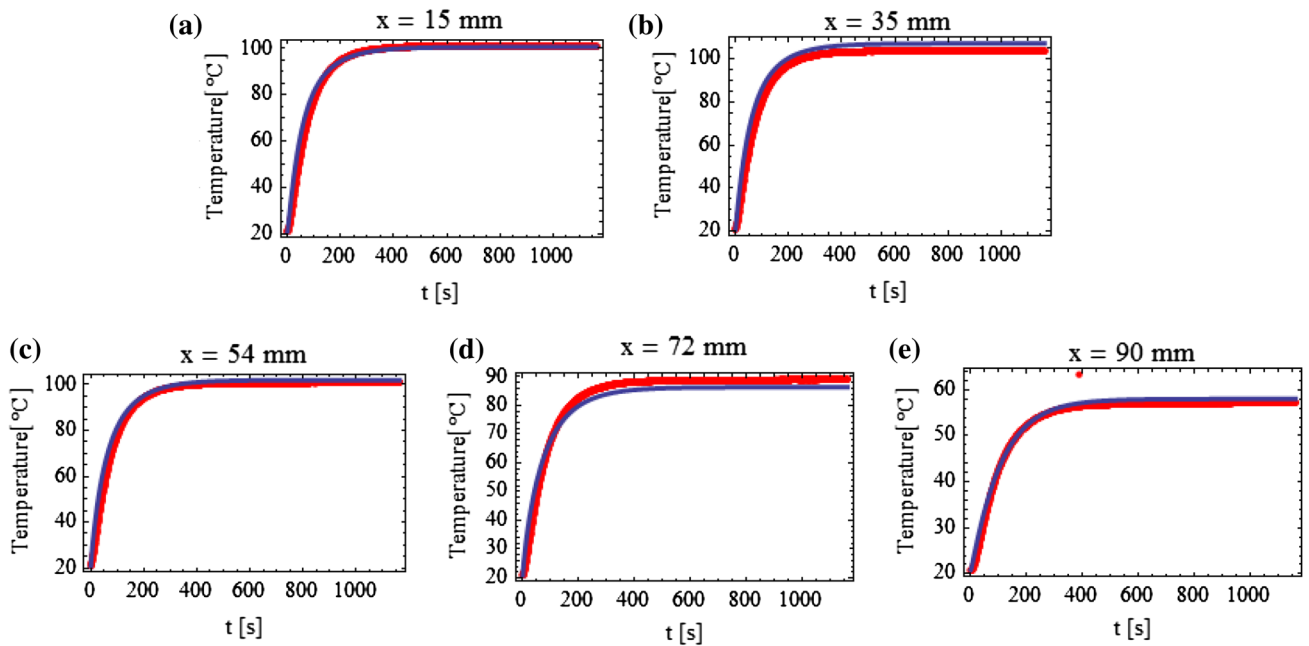

Fig. 11 Comparison between the time evolution of measured (*red*) and simulated (*blue*) temperatures at different positions along the Pitot probe length, for the DINAM-INMETRO wind tunnel experiments (color figure online)

longitudinal coordinate. The agreement between the two sets of results is again excellent, giving confidence that the conjugated model is perfectly capable of accurately describing the transient behavior of the temperature field along the Pitot tube. However, if the porcelain electrical insulation is not accounted for in the effective thermophysical properties, particularly in the local thermal capacity, significant deviations between experimental and theoretical results are observed, as discussed in [26, 28].

Next, the climatic wind tunnel (NIDF-COPPE) was employed in the validation of the Pitot probe model, for

a more challenging transient situation, by promoting successive step changes in the power generation of the probe heating system, corresponding to on–off cycles of about the same period. Both thermocouple and infrared thermography temperature measurements were recorded for comparison purposes. The results here reported correspond to a fan rotation of 800 rpm, which corresponded to a free stream air velocity of 22.87 m/s at the test section. In the beginning of the test, the air temperature was at 8.7 °C, increasing along the experiment to 10.8 °C. Figure 12a shows the applied electrical power applied to the heating system, for

1502

J Braz. Soc. Mech. Sci. Eng. (2016) 38:1489–1509

(a)

(b)
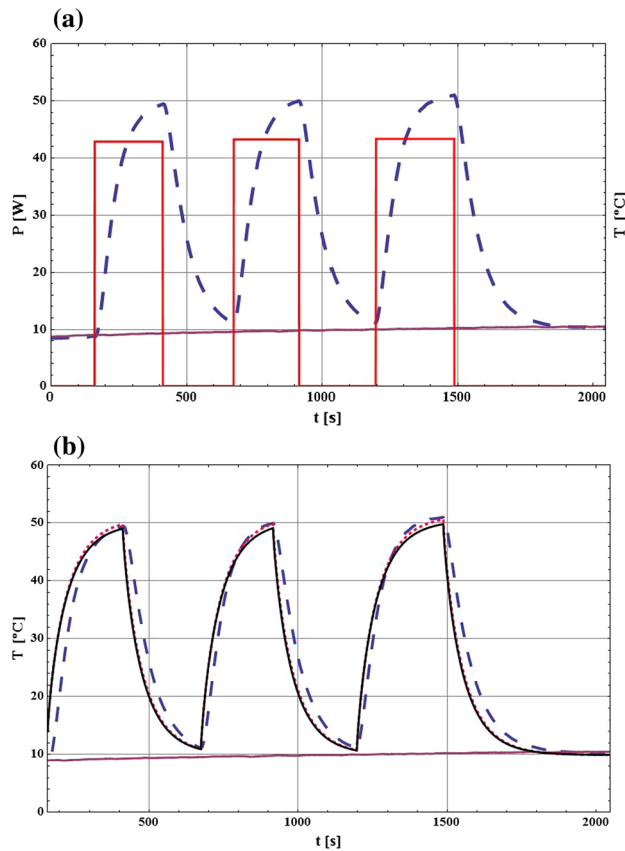
Fig. 12 a Transient power generation in probe and achieved measured temperature transient at 80 mm. Temperature of air in the tunnel, lower line *purple*. (800 rpm—22.87 m/s).**b** Comparison between the theoretical and experimental transient temperature fields: experimental in *red*, and theory in *black-yellow* (color figure online)

a maximum voltage difference of 52 V, with a behavior that approximates the transients promoted by the pilot in the A4 flight tests that will be discussed in what follows. The temperature measurements at a position of 80 mm from the probe tip are also presented. Figure 12b then provides a comparison of the same temperature measurements at $x = 80$ mm, in red, and the theoretical predictions, for both the classical lumped and improved lumped models, in black and yellow, respectively. The air temperature within the test section is also provided in the lower violet curve. An excellent agreement between the theoretical curves is achieved, as well as with the experimental temperature evolution, with a slightly faster thermal response being predicted by the proposed model.

6.2 Validation for compressible flow: A4 flight tests

In [28, 32], flight tests were reported in a A-4 Skyhawk aircraft of the VF-1 Squadron, in the Brazilian Aero-Naval Base, at São Pedro d´Aldeia, Rio de Janeiro, in order to

determine the thermal behavior of an instrumented Pitot tube under actual flight conditions and thus validate the models developed for compressible flow situations. In order to generate abrupt transient variations, the A4 pilot was required to repeatedly turn on and off the Pitot thermal protection system, thus allowing for the observation of the thermal response of the probe to sudden heat transfer perturbations. Two flights were here selected for analysis, the first with a Mach number of 0.5 and at 10,000 ft of altitude, and the second one with a Mach number of 0.51 and at 15,000 ft of altitude.

Figure 13 shows the predicted transient behavior of the Pitot probe temperature at a point located 80 mm from the stagnation point, accounting for the influence of the porcelain's heat capacity in the time response. Both the classical lumping (red curves) and improved lumped (black curves) procedures have been included in this comparison. The experimental thermocouple readings are plotted in blue, while the measured external air temperature is shown in green lines. It can be noticed that the model slightly under-predicts the time necessary to reach steady state after each switching cycle at the lower altitude, with a closer agreement in the higher altitude flight. Another worthy observation is that for the 10,000 ft flight, the two lumping approaches differ more noticeably, with the improved lumped approach yielding better results. This is due to the fact that the heat transfer coefficients are higher at the lower altitude flight, i.e., higher velocities and denser air, and thus, the Biot numbers tend to be higher in this case, which favors the use of the improved lumped analysis for higher accuracy.

Steady-state theoretical results for the A4 flights have also been analyzed, by comparing the simple thermal model using correlations for the external heat transfer coefficient [26], against the complete conjugated problem here described. Figure 14 shows that the uncoupled model (in red) overestimates the probe surface temperatures at the stagnation and tip regions in both flight situations, to within 5 °C in comparison to the full conjugated model (in black). This result reconfirms the importance of taking into account the mutual influence between the solid and the fluid and the need for a conjugated model to more accurately describe the thermal behavior of the Pitot tube under critical conditions.

6.3 Flight in icing conditions: Pitot probe

In the following simulation, we have used the data relative to the PH510 but with conditions close to those for the AF 447 flight, as provided in the final report of the BEA, French Agency responsible for the accident investigation. The conditions adopted were altitude of 11 km and Mach number between 0.82 and 0.86 (871–913 km/h).
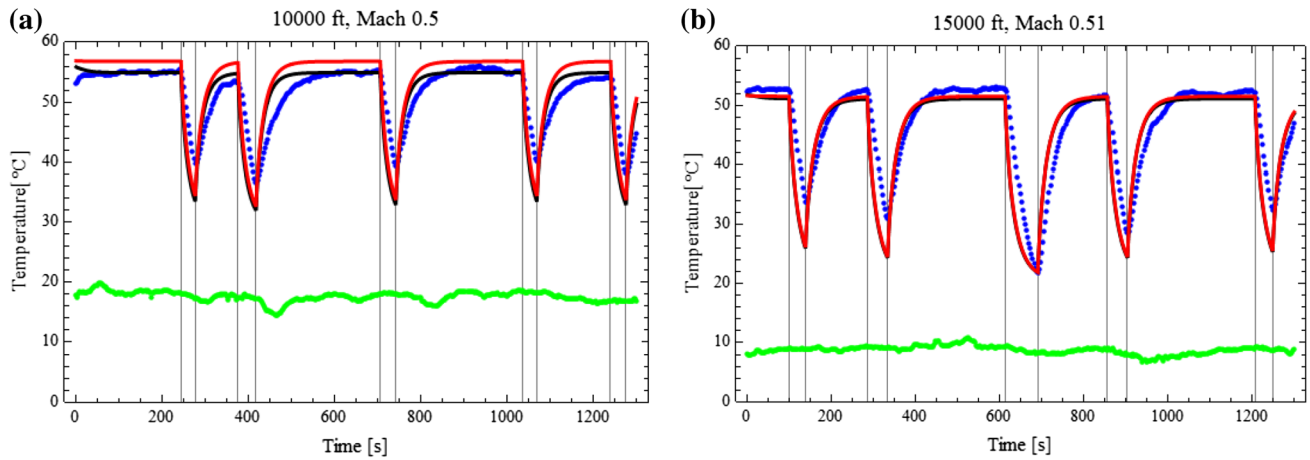
Fig. 13 Time evolution of the temperature at the surface of the Pitot distant 80 mm from the stagnation point, considering the porcelain influence, with improve lumped model, in *black*, with classical lumped model, in *red*, and with experimental results, in *blue*: **a** flight at 10,000 ft and Mach 0.5; **b** flight at 15,000 ft and Mach 0.51 (color figure online)
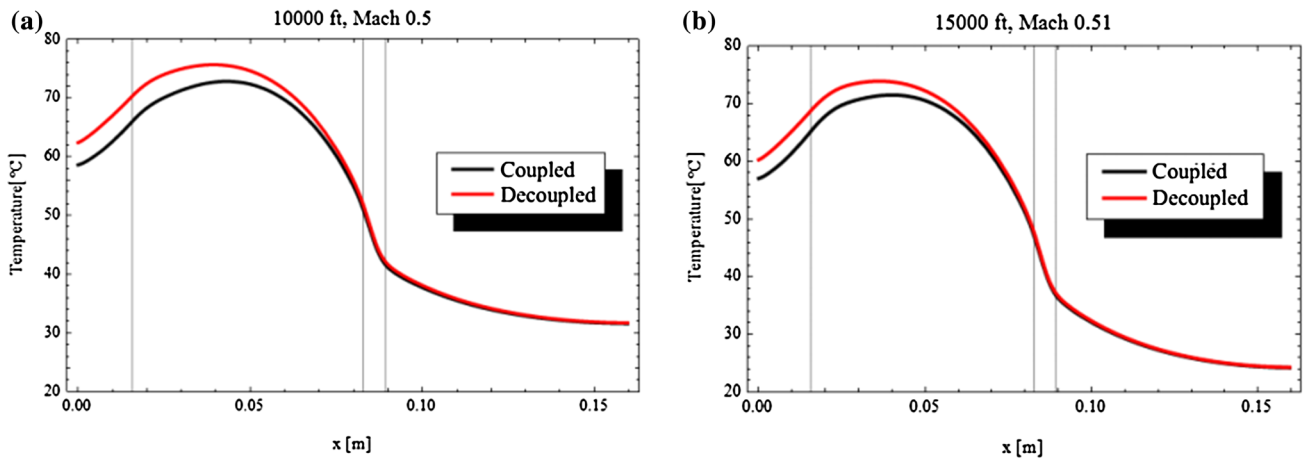

Fig. 14 Temperature distribution along longitudinal position in steady state: **a** flight at 10,000 ft and Mach 0.5; **b** flight at 15,000 ft and Mach 0.51(coupled model in *black line*, decoupled model in *red line*) (color figure online)

Here, the improved lumped model for the Pitot energy equation was solved with correlations for the heat transfer coefficients and the modified Messinger model for the ice accretion [31, 49]. Figure 15a illustrates the transient behavior of the temperature distribution along the surface of the Pitot probe, where clearly it is observed that the temperature at the stagnation region achieves values below freezing temperature during the time interval investigated. Figure 15b shows the time evolution of the temperature at the stagnation region, which allows one to evaluate that after about 2000s icing starts (about 33 min). This time is very close to the period of 30 min that appears in the BEA report, pointed out as the time elapsed after the A330 entrance into the cloud formation until the beginning of the probes freezing. These results considered only the liquid part of the water in LWC, with assumed values of

LWC = 1.115 g/m^3, MVD = 45 μm, and ice crystals were not accounted for.

Figure 16a shows a prediction of ice formation on the Pitot tube PH-510, for the conditions $u_\infty = 56$ m/s, LWC = 0.59 g/m^3, $T_{sur} = -10$ °C, MVD = 26.2 μm. From the ice shape, it can be observed that the accretion occurs mainly at the stagnation region, with a distinct reduction along the conical region and no occurrence in the cylindrical region. The simplified ice formation model is obtained from airfoil equations and then geometry factors and collection efficiency relations are adopted for the Pitot tube in stagnation line and conical region. The ice accretion on the conical region and beyond is negligible due to the very small value of the collection efficiency ($\beta < 0.2$). Although experimental and theoretical analyses of ice formation on Pitot tubes were not yet available in the open literature, we

(a)

(b)
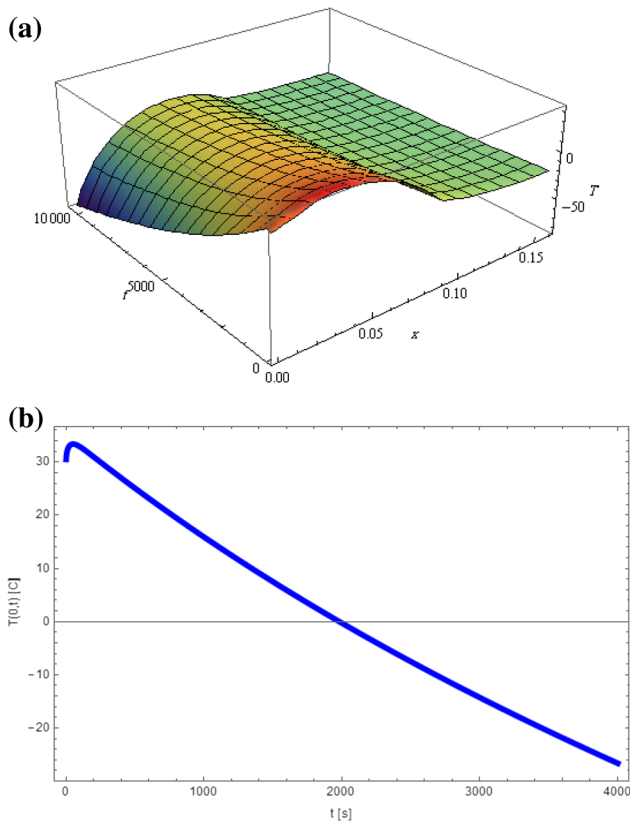
Fig. 15 a Theoretical prediction of temperatures along the probe PH510 before and after starting icing in situation of flight with ice formation ($T_\infty = -54$ °C, LWC = 1.115 g/m³, MVD = 45 μm, $u_\infty = 800$ km/h). **b**. Transient behavior of the temperature in the stagnation region of the Pitot probe in situation of flight with ice formation ($T_\infty = -54$ °C, LWC = 1.115 g/m³, MVD = 45 μm, $u_\infty = 800$ km/h)
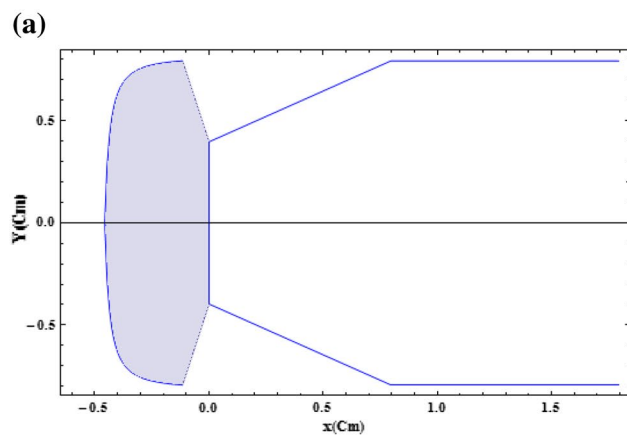
have obtained from private communication with the TsAGI Climatic Icing Wind Tunnel, Russia, some sample images from their Pitot tube icing experiments, as displayed in Fig. 16b. TsAGI has a climatic wind tunnel for investigations of aircraft parts and aviation materials at icing conditions. From a qualitative point of view, one can conclude that the ice shape in these images indicates that the present simulation is apparently consistent with the expected physical behavior on ice accretion.

6.4 Flight in icing conditions: wing section

One of the difficulties encountered in the present effort on the analysis of anti-icing systems for Pitot probes was the lack of previous works in the open literature for comparison purposes, in either simulation or experimentation of icing of Pitot tubes or any other aeronautical sensor. Therefore, it became essential to verify and validate the proposed fully local differential formulation, with the single-domain formulation strategy and including the modified Messinger model for ice accretion, in the case of icing of airfoils, for which the literature is much richer. A substantial amount of information and studies about wing, empennage, and engine intake icing can be readily found in the open literature, in light of the commercial and strategic advantages that such knowledge can provide. Controlled distribution software was developed throughout recent years, such as LEWICE, ONERA2D, TRAJICE, CANICE, and many others [50, 51]. Even though the importance of studying the icing of Pitot tubes is well recognized for the reasons already discussed, very little information concerning this particular subject was found in the open literature, possibly

(a)

(b)

Fig. 16 a Ice shape in the Pitot probe PH-510 under conditions $u_\infty = 56$ m/s, LWC = 0.59 g/m³, $T_{sur} = -10$ °C, MVD = 26.2 μm. **b**. Ice shape over Pitot probe as obtained in the TsAIG Climatic Icing

Wind Tunnel, Russia (Prof. Ivan Egorov, Head of TsAGI research department, private communication)

J Braz. Soc. Mech. Sci. Eng. (2016) 38:1489–1509

1505

Case	U_∞ (m/s)	α	T_∞ (K)	LWC (g/m³)	MVD (μm)	Total time (s)
C14	57.0	0°	267.6	1.04	27.73	247.2

Table 2 Conditions for test with ice formation over wing section [52]

(a)

(b)
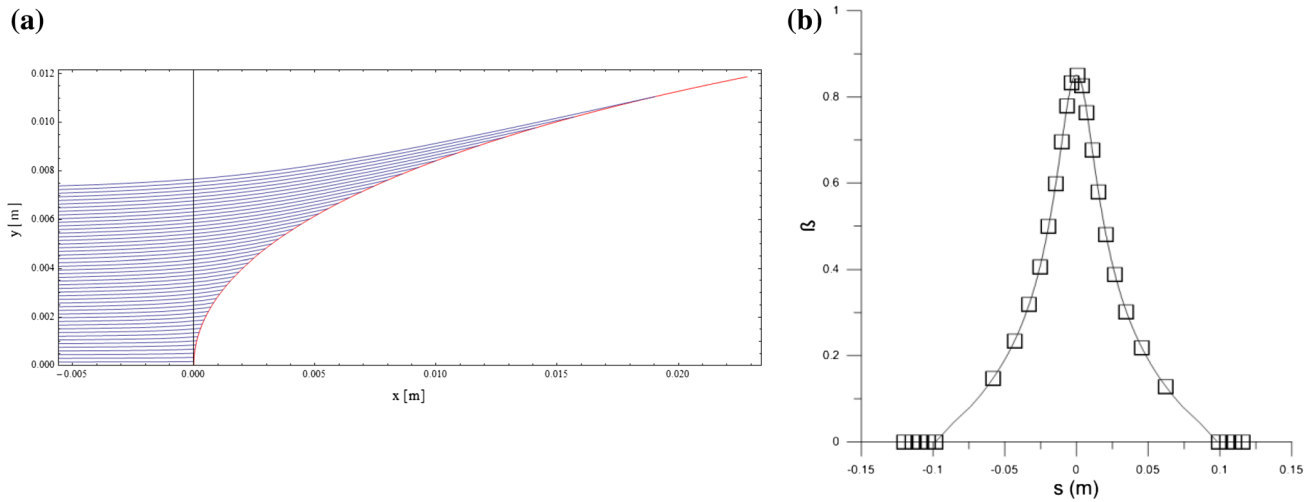
Fig. 17 a Trajectories and impact points of supercooled droplets in case C14. **b** Collection efficiency for case C14

due to commercial issues or to a minimized importance in comparison with icing problems on other, supposedly, more vital aircraft components.

In order to validate the results obtained in [39] for ice formation over airfoils, the experimental results in [52] have been considered. This experimental work employs a NACA 0012 airfoil with chord of 0.27 m, without any active anti-icing system, under appropriate conditions for ice accretion. Table 2 summarizes the relevant input data for this simulation, employing the fully local differential model for the conjugated problem discussed above, together with the modified Messinger model.

For the conditions of case C14 from [52], the trajectories of the supercooled water droplets have been computed. Figure 17a shows the result of the Lagrangian simulation of the trajectories of 50 droplets, with the corresponding impact points over the airfoil surface. Figure 17b provides the collection efficiency calculated from these simulated trajectories, where fairly significant coefficients are obtained up to 10 cm away from the stagnation point, in part due to the fairly high values of the liquid water content (LWC) and of the mean value diameter (MVD) of the droplets.

After solving both the flow and conjugated heat transfer problems with the single-domain formulation, the modified Messinger model [36–38] is employed to estimate the ice accretion process. Only then the ice layer profile predicted by the present model (external black curve) can be critically compared with the experimental results in [52] (blue curve)

and the simulation in [53] (red curve), as shown in Fig. 18. It can be seen that the two simulations are fairly close to each other, along most of the airfoil length where the collection efficiency has representative values, and some deviation between the two simulations is noticeable only at the end of the wing section, possibly due to some slight differences in the calculation methodology for the collection efficiency. Both theoretical results have noticeable deviations from the experimental ice layer profile, though following the same overall behavior, possibly because the various impinging water flow regimens have not been considered. It should also be mentioned that the present model does not account for the influence of the ice layer or water film in the external convection, and thus, the heat transfer coefficient is not updated once ice accretion is observed.

6.5 Velocity and heat transfer coefficient estimation

The estimation of $h_e^k \equiv h_e(t_k)$ and $u_\infty^k \equiv u_\infty(t_k)$ with the SIR algorithm presented above was examined by using simulated temperature measurements of sensors located at $x = 0.005$ m and $x = 0.06$ m. These positions were selected so that the first one was relatively close to the tip of the Pitot tube and, therefore, with readings more significantly affected by the heat transfer coefficient at this region. The second sensor was assumed to be located in the region where the perimeter of the Pitot tube does not vary. The readings of this sensor are expected to be more sensitive to variations in the heat transfer coefficient over the lateral

1506

J Braz. Soc. Mech. Sci. Eng. (2016) 38:1489–1509

Fig. 18 Ice layer profiles for case C14: airfoil profile (*internal black curve*); present model (*external black curve*); experimental [44] (*blue curve*); numerical simulation [45] (*red curve*) (color figure online)
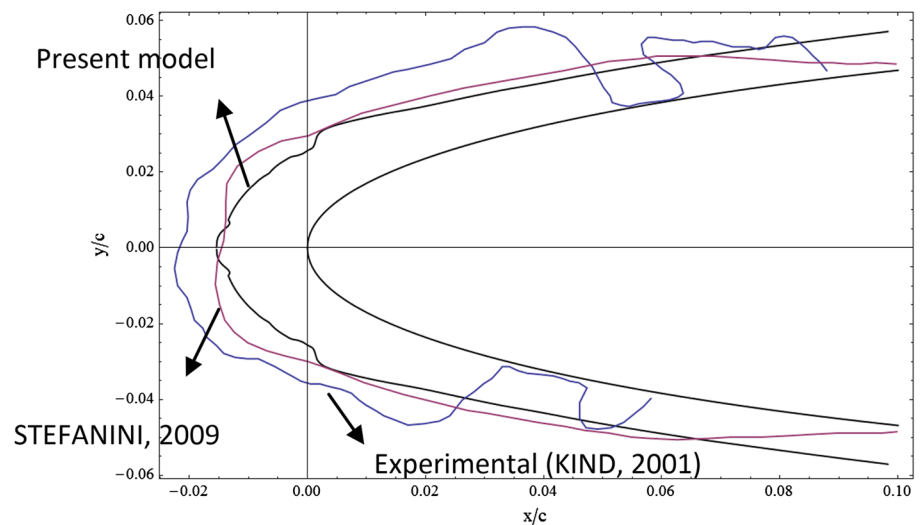
Fig. 19 Test case for inverse analysis of velocity and heat transfer coefficient estimation. **a** Exact functional form for $h_e(t)$. **b** Functional form for $u_\infty(t)$ in test case
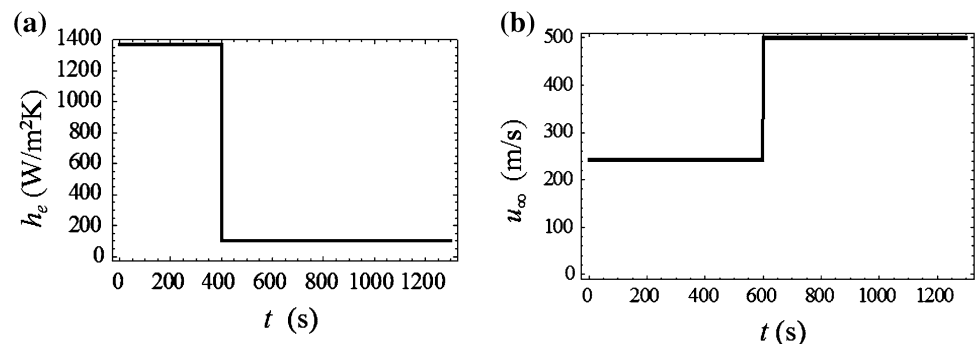

surface of the Pitot tube, which is highly dependent on the relative air speed u_∞. Temperature measurements were supposed to be available every 10 s. In order to generate the simulated measurements, the direct problem was solved with 2000 grid points, and by specifying functional forms for h_e^k and u_∞^k. The heat transfer coefficient at the tip of the Pitot tube was supposed to be 1380 W/m²K, for the base speed of 243 m/s [28] and then to drop to 100 W/m²K after the formation of ice layers over this region, as a simplified test model for the heat transfer at the sensor tip, which was supposed to begin at time $t = 400$ s. The functional form for $h_e(t)$ is illustrated in Fig. 19a. For the relative speed $u_\infty(t)$, three different cases were examined in [47], involving a sudden increase in the form of a step function, as well as periodic behaviors with discontinuities in the first derivative of the function and in the function itself. Only the case for a step change in the air speed is here presented, as shown in Fig. 19b. Note that the speed variations were supposed to start at time $t = 600$ s, that is, after the ice accretion began.

The simulated data noise was additive, Gaussian, with zero mean and a constant standard deviation of 5 % of the maximum measured temperature. The simulated

measurements for the test cases are presented in Fig. 20 (red dots), together with the exact temperature variation obtained from the solution of the direct problem (blue lines). An analysis of Fig. 20 reveals that the temperature at the position $x = 0.005$ m suddenly increased at $t = 400$ s when the ice layer was formed ($h_e(t)$ dropped to 100 W/m²K). On the other hand, the temperature at $x = 0.06$ m was very little affected by this sudden drop in $h_e(t)$. The temperatures at both positions increased when the relative speed $u_\infty(t)$ increased, as a result of an increase in the adiabatic wall temperature. Figure 20 also shows that the simulated measurement errors are significantly larger than the temperature variations resulting from the decrease in $h_e(t)$.

The results obtained for the estimation of $h_e(t)$ and $u_\infty(t)$, with 250 and 500 particles in the SIR algorithm of the particle filter, are presented by Fig. 21a, b and Fig. 21c,d, respectively. The results are presented in terms of the means of the state variables (red stars) and their 99 % confidence intervals (blue crosses). The exact functional forms are also shown in these figures by green lines. These figures show that, in general, even with such small numbers of particles used in the SIR algorithm and with measurements with large errors, the unknown functions can be

J Braz. Soc. Mech. Sci. Eng. (2016) 38:1489–1509

1507
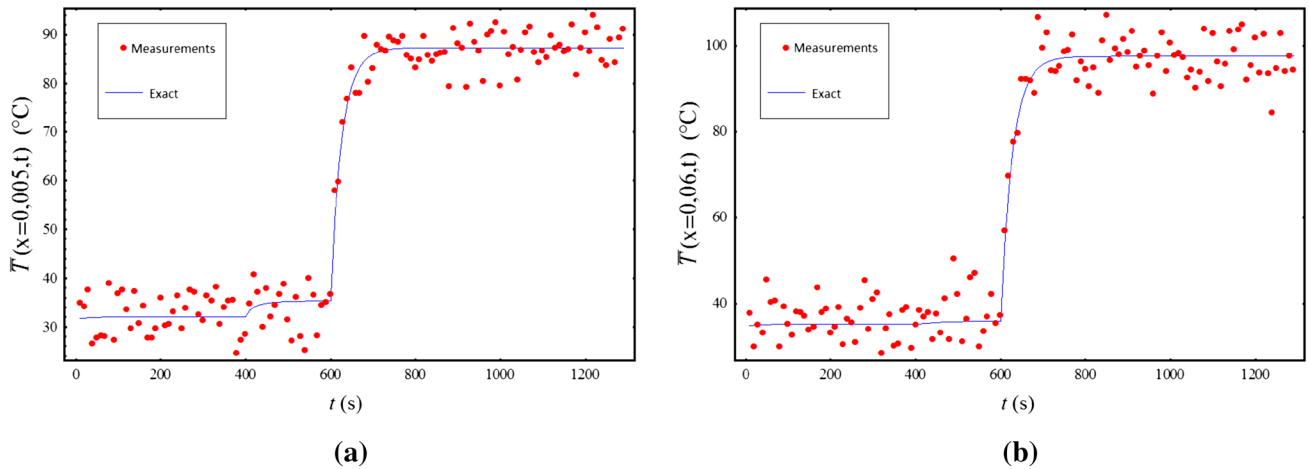
Fig. 20 Simulated measurements (*red dots*) and exact temperatures (*blue lines*) at positions. **a** $x = 0.005$ m and **b** $x = 0.06$ m for test case (color figure online)
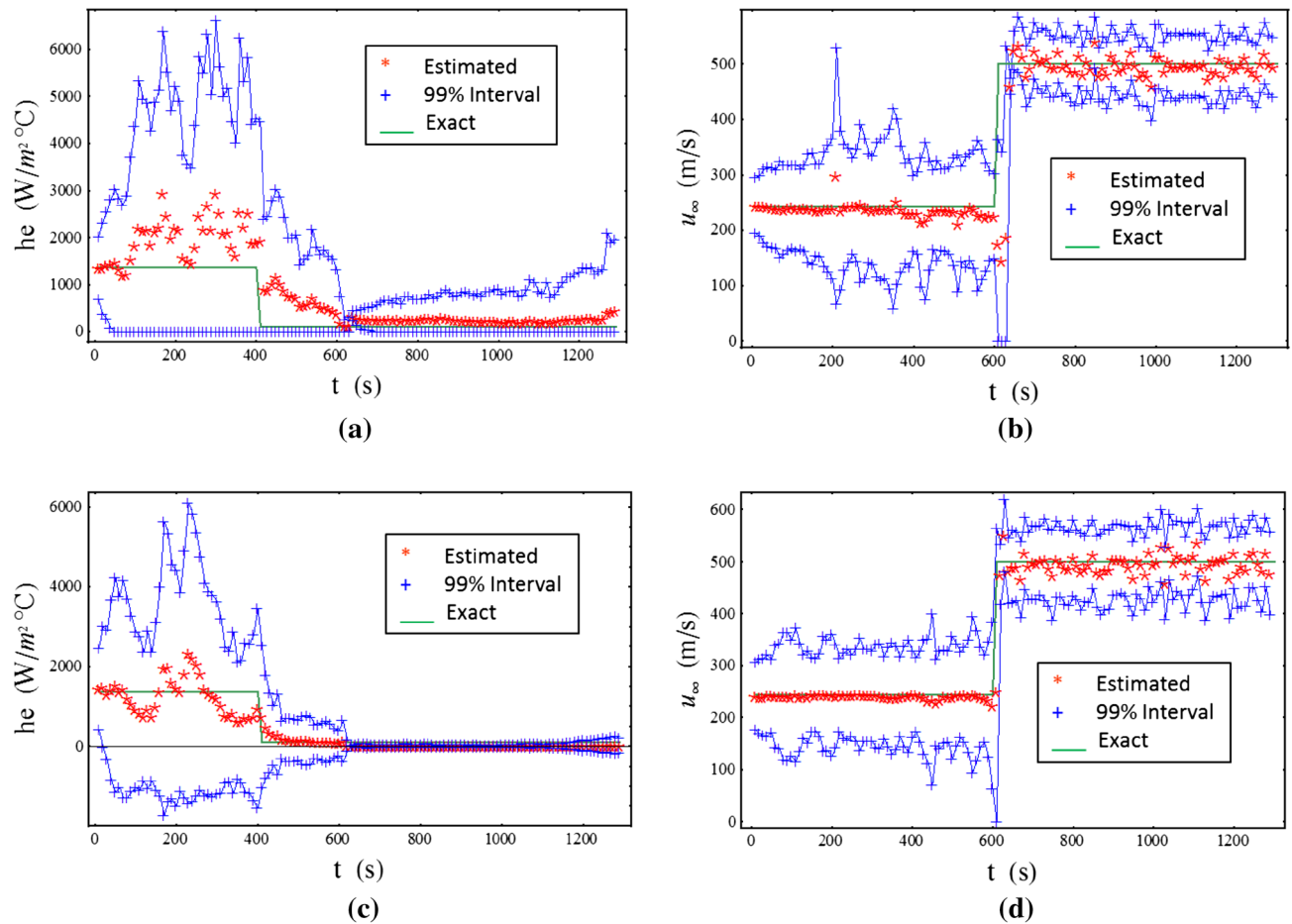
Fig. 21 Results for the heat transfer coefficient and velocity estimations for the test case obtained with **a**, **b** 250 particles and **c**, **d** 500 particles—means of the state variables (*red stars*), 99 % cred-ible intervals (*blue crosses*) and exact functional forms (*green lines*). **a** and **c** h_e. **b** and **d** u_∞ (color figure online)

recovered quite well. The jumps in the functions containing discontinuities are estimated after some delay, caused by the random walk standard deviations used in this work, which were selected so that smooth solutions could be estimated. In fact, faster responses of the estimated functions after discontinuities in the exact functions could be

1508

J Braz. Soc. Mech. Sci. Eng. (2016) 38:1489–1509

obtained, but at the expense of unstable behaviors, caused by the ill-posed character of the inverse problem. It is also interesting to notice in Fig. 21 that the sudden decrease in $h_e(t)$, caused by the ice layers that are formed over the tip of the Pitot tube, could be accurately identified, despite the fact that the measurement errors are larger than the exact temperature variation resulting from the variation in such heat transfer coefficient. On the other hand, such a fact yields confidence intervals for $h_e(t)$ much larger than those for $u_\infty(t)$.

7 Conclusions

The results here obtained and critically compared to both incompressible and compressible flow experiments demonstrated that the developed conjugated heat transfer model and associated hybrid solution methodologies are capable of accurately predicting the transient thermal behavior of aeronautical Pitot tubes with anti-icing systems, in both controlled laboratory wind tunnel experiments and in actual airplane flights. The model here validated by the wind tunnels and A4 flight experimental data was then employed in the analysis of more severe conditions that may lead to ice formation, as the basic heat transfer formulation for the incorporation of a well-accepted ice accretion model.

Future work includes the validation of the complete model of conjugated heat transfer with ice accretion for the Pitot probe, under controlled tests in the climatic wind tunnel of NIDF-COPPE/UFRJ, due to the lack of experimental studies on this matter [54]. Also, predictive tools for velocity estimation based solely on temperature measurements, through the use of particle filters within the Bayesian framework, should now be tested against actual wind tunnel data. The goal is to provide an alternative and concurrent velocity estimation procedure, sufficiently robust to provide reliable estimations even under icing, but employing the conventional Pitot probes with an installed temperature sensor.

References

1. Luikov AV, Aleksashenko VA, Aleksashenko AA (1971) Analytical methods of solution of conjugated problems in convective heat transfer. Int J Heat Mass Transf 14:1047–1056
2. Luikov AV (1974) Conjugate convective heat transfer problems. Int J Heat Mass Transf 17(2):257–265
3. Perelman TL (1961) On conjugated problems of heat transfer. Int J Heat Mass Transf 3:293–303
4. Cotta RM (1990) Hybrid numerical-analytical approach to nonlinear diffusion problems. Num Heat Transf Part B 127:217–226
5. Cotta RM (1993) Integral transforms in computational heat and fluid flow. CRC Press, Boca Raton
6. Cotta RM, Mikhailov MD (1997) Heat conduction: lumped analysis, integral transforms, symbolic computation. Wiley-Interscience, Chichester
7. Cotta RM (1998) The integral transform method in thermal and fluids sciences and engineering. Begell House, New York
8. Cotta RM, Mikhailov MD (2006) Hybrid Methods and Symbolic Computations. In: Minkowycz WJ, Sparrow EM, Murthy JY (eds) Handbook of numerical heat transfer, 2nd edn, chap 16. Wiley, New York
9. Guedes ROC, Cotta RM, Brum NCL (1991) Heat transfer in laminar tube flow with wall axial conduction effects. J Thermophys Heat Transf 5(4):508–513
10. Guedes ROC, Cotta RM (1991) Periodic laminar forced convection within ducts including wall heat conduction effects. Int J Eng Sci 29(5):535–547
11. Naveira CP, Lachi M, Cotta RM, Padet J (2009) Hybrid formulation and solution for transient conjugated conduction–external convection. Int J Heat Mass Transf 52(1–2):112–123
12. Nunes JS, Cotta RM, Avelino MR, Kakaç S (2010) Conjugated heat transfer in microchannels. In: Kakaç S, Kosoy B, Pramuanjaroenkij A (eds) NATO science for peace and security series A: chemistry and biology, microfluidics based microsystems: fundamentals and applications. pp 61–82
13. Knupp DC, Naveira-Cotta CP, Cotta RM (2012) Theoretical analysis of conjugated heat transfer with a single domain formulation and integral transforms. Int Commun Heat Mass Transf 39(3):355–362
14. Knupp DC, Naveira-Cotta CP, Cotta RM (2013) Conjugated convection–conduction analysis in micro-channels with axial diffusion effects and a single domain formulation. ASME J Heat Transf (Special Issue on Micro/Nanoscale Heat and Mass Transfer) 135(9):091401–091411
15. Knupp DC, Cotta RM, Naveira-Cotta CP (2013) Heat transfer in microchannels with upstream-downstream regions coupling and wall conjugation effects. Num Heat Transf Part B Fundam 64:365–387
16. Knupp DC, Cotta RM, Naveira-Cotta CP, Kakaç S (2015) Transient conjugated heat transfer in microchannels: integral tranforms with single domain formulation. Int J Therm Sci 88:248–257
17. Knupp DC, Naveira-Cotta CP, Cotta RM (2014) Theoretical-experimental analysis of conjugated heat transfer in nanocomposite heat spreaders with multiple micro-channels. Int J Heat Mass Transf 74:306–318
18. Knupp DC, Cotta RM, Naveira-Cotta CP (2015) Fluid flow and conjugated heat transfer in arbitrarily shaped channels via single domain formulation and integral transforms. Int J Heat Mass Transf 82:479–489
19. Cotta RM, Quaresma JNN, Sphaier LA, Naveira-Cotta CP (2010) Unified integral transform approach in the hybrid solution of multidimensional nonlinear convection–diffusion problems.

14th International heat transfer conference, vol 2, paper no IHTC14-22396, pp 477–486, Washington, DC

20. Sphaier LA, Cotta RM, Naveira-Cotta CP, Quaresma JNN (2011) The UNIT algorithm for solving one-dimensional convection–diffusion problems via integral transforms. Int Commun Heat Mass Transf 38(5):565–571

21. Cotta RM, Knupp DC, Naveira-Cotta CP, Sphaier LA, Quaresma JNN (2013) Unified integral transforms algorithm for solving multidimensional nonlinear convection–diffusion problems. Num Heat Transf Part A Appl 63:1–27

22. Cotta RM, Knupp DC, Naveira-Cotta CP, Sphaier LA, Quaresma JNN (2014) The unified integral transforms (UNIT) algorithm with total and partial transformation. Comput Therm Sci 6(6):507–524

23. Wolfram S (2008) The *Mathematica* book. Wolfram Media, Cambridge

24. Gent RW, Dart NP, Cansdale JT (2000) Aircraft icing. Philos Trans R Soc Lond A 358:2873–2911

25. Caliskan F, Aykan R, Hajiyev C (2008) Aircraft icing detection, identification, and reconfigurable control based on kalman filtering and neural networks. J Aerosp Eng 21(2):51–60

26. Souza JRB, Zotin JLZ, Loureiro JBR, Naveira-Cotta, CP, Silva Freire AP, Cotta RM (2011) Conjugated heat transfer analysis of heated Pitot tubes: wind tunnel experiments, infrared thermography and lumped-differential modeling. 21st International congress of mechanical engineering, COBEM-2011, ABCM, Natal, October 2011

27. Lisboa KM, Souza JRB, Cotta RM, Naveira-Cotta CP (2012) Transient conjugated heat transfer in external compressible laminar flow over plates with internal heat generation. VII National congress of mechanical engineering, CONEM 2012, São Luis, pp 1–10, 31st July–3rd August, 2012

28. Souza JRB, Lisboa KM, Cerqueira IG, Naveira-Cotta CP, Cotta RM, Zotin JLZ (2012) Conjugated heat transfer models for heated aeronautical Pitot tubes: experimental validation with A4 Skyhawk flight tests. 14th Brazilian congress of thermal sciences and engineering, ENCIT 2012, Rio de Janeiro, November, 2012

29. Lisboa KM, Souza JRB, Cotta RM (2013) Thermal analysis of an aeronautical Pitot probe with anti-icing system: modeling, simulation and parametric studies. In: Proceedings of the 22nd international congress of mechanical engineering—COBEM 2013, Ribeirão Preto, November 3–7, 2013

30. Lisboa KM, Cotta RM (2014) External flow conjugated problem analysis via integral transforms and single domain formulation. 3rd International conference on computational methods for thermal problems—ThermaComp2014, Lake Bled, June, 2014

31. Allahyarzadeh AB, Souza JRB, Lisboa KM, Cotta RM (2015) Thermal analysis of heated Pitot probes in atmospheric conditions of ice accretion. In: Proceedings of the 23rd international congress of mechanical engineering—COBEM 2015, Rio de Janeiro, RJ, Brazil, December 6th–10th, 2015

32. Souza JRB, Lisboa KM, Cerqueira IG, Naveira-Cotta CP, Cotta RM, Zotin JLZ (2015) Conjugated heat transfer analysis of heated aeronautical Pitot probes with flight tests experimental validation. Heat Transf Eng 36:991–1000

33. Ozisik MN, Mikhailov MD (1984) Unified analysis and solutions of heat and mass diffusion. Wiley, New York

34. Cebeci T, Cousteix J (2005) Modeling and computation of boundary layer flows, 2nd edn. Springer, Berlin

35. Schlichting H, Truckenbrodt E (1979) Aerodynamics of the airplane, 1st edn. McGraw-Hill, New York

36. Myers TG (2001) Extension to the Messinger model for aircraft icing. AIAA J Am Inst Aeronaut Astronaut 39(2):211–218

37. Myers TG, Charpin JPF, Thompson CP (2002) Slowly accreting ice due to super cooled water impacting on a cold surface. Phys Fluids 14(1):240–256

38. Özgen S, Canibek M (2009) Ice accretion simulation on multi-element airfoils using extended Messinger model. Heat Mass Transf 45(3):305–322

39. Lisboa KM (2015) Model for ice formation over heated aeronautical surfaces: potential flow, differential boundary layer model and single domain formulation. MSc thesis, COPPE-UFRJ

40. West M (1993) Approximating posterior distributions by mixture. J R Statist Soc B 55:409–422

41. Pitt M, Shephard N (1999) Filtering via simulation: auxiliary particle filters. J Am Statist Assoc 94(446):590–599

42. Doucet A, Freitas N, Gordon N (2001) Sequential Monte Carlo methods in practice. Springer, New York

43. Arulampalam S, Maskell S, Gordon N, Clapp T (2001) A tutorial on particle filters for on-line non-linear/non-Gaussian Bayesian tracking, IEEE, 18 p

44. Kaipio J, Somersalo E (2004) Statistical and computational inverse problems, applied mathematical sciences. Springer, Berlin

45. Ristic B, Arulampalam S, Gordon N (2004) Beyond the Kalman filter—particle filter for tracking applications. Artech House, Norwood

46. Orlande HRB, Colaço MJ, Dulikravich G, Vianna F, Silva WB, Fonseca H, Fudym O (2012) State Estimation Problems In Heat Transfer. International Journal for Uncertainty Quantification 2(3):239–258

47. Andrade GJA, Orlande HRB, Cotta RM (2014) Use of particle filters to estimate relative air speed in a Pitot tube. ICCHMT international symposium on convective heat and mass transfer in sustainable energy, CONV-14, Kusadasi, Turkey, June 2014

48. Souza JRB (2014) Theoretical-experimental thermal analysis of aeronautical Pitot probes, wind-tunnel experiments, in flight testing and basic design of UFRJ climatic wind tunnel. DSc thesis, COPPE-UFRJ

49. Bidgoli AA (2013) Thermal analysis of aeronautical Pitot tubes with ice formation. MSc thesis, COPPE-UFRJ

50. Silva GAL, Silvares OM, Zerbini EJGJ (2007) Numerical simulation of airfoil thermal anti-ice operation part 1: mathematical modeling. J Aircr 44(2):627–633

51. Stefanini LM, Silvares OM, Silva GAL, Zerbini EJGJ (2008) Boundary-layers integral analysis—airfoil icing, AIAA paper 2008-0474. Aerospace sciences meeting and exhibit, 46th, 2008, Reno, American Institute of Aeronautics and Astronautics, Reston

52. Kind R (2001) Ice accretion simulation evaluation test, North Atlantic Treaty Organization—Research and Technology Organisation—NATO-RTO. Technical report 038, 32 p

53. Stefanini LM (2009) Effect of the thermal boundary layer on the ice formation over aeronautical airfoils. MSc thesis, Universidade de São Paulo, USP, São Paulo

54. Silva GAL (2010) Similarity studies for air data probes new standard—AS5562. Coupled heat and mass transfer effects, SAE AC-9C Aircraft Icing Technology Committee meeting October 8th–10th 2010—Portland